Steady-State Modeling of Modular Multilevel Converter Under Unbalanced Grid Conditions

Xiaojie Shi, *Student Member, IEEE*, Zhiqiang (Jack) Wang, *Member, IEEE*, Bo Liu, *Student Member, IEEE*,
Yalong Li, *Student Member, IEEE*, Leon M. Tolbert, *Fellow, IEEE*, and Fred Wang, *Fellow, IEEE*

***Abstract*—This paper presents a steady-state model of MMC for the second-order phase voltage ripple prediction under unbalanced conditions, taking the impact of negative-sequence current control into account. From the steady-state model, a circular relationship is found among current and voltage quantities, which can be used to evaluate the magnitudes and initial phase angles of different circulating current components. Moreover, in order to calculate the circulating current in a point-to-point MMC-based HVdc system under unbalanced grid conditions, the derivation of equivalent dc impedance of an MMC is discussed as well. According to the dc impedance model, an MMC inverter can be represented as a series connected *R–L–C* branch, with its equivalent resistance and capacitance directly related to the circulating current control parameters. Experimental results from a scaled-down three-phase MMC system under an emulated single-line-to-ground fault are provided to support the theoretical analysis and derived model. This new models provides an insight into the impact of different control schemes on the fault characteristics and improves the understanding of the operation of MMC under unbalanced conditions.**

***Index Terms*—DC equivalent impedance, high-voltage direct-current (HVdc), modular multilevel converter (MMC), single-line-to-ground (SLG) fault, steady-state analysis, unbalanced conditions.**

I. INTRODUCTION

FEATURING low switching frequency, modular design, high output voltage quality, compact size, etc., modular multilevel converters (MMCs) have become a promising technology for high-voltage direct-current (HVdc) transmission systems to transmit power from far away locations, like offshore wind farms, to main ac power grids [1]–[3].

The steady-state and dynamic analysis of MMC under normal operation have been thoroughly discussed in the existing literature, using large-signal and/or small-signal models [4]–[6]. Based on these models, system parameters, such as arm inductance and submodule (SM) capacitance can be designed [7], [8]. Moreover, the operation principle and design considerations of circulating current suppression as well as capacitor voltage balancing control schemes can be further understood [9]–[11].

Under unbalanced grid conditions, most previous research efforts focused on proving the existence of zero-sequence double-line frequency active power, which will flow into the dc side and cause dc voltage and/or dc current ripples. References [12] and [13] give the analytical relationship among instantaneous active/reactive power and fundamental frequency positive- as well as negative-sequence voltage and current in ac terminals. According to this relationship, the current references for active power ripple elimination can be calculated. The relationship, however, does not take the second-order components in both circulating current and capacitor voltages into account, and cannot fully describe the ac fault characteristics inside the MMC. As an improvement, instantaneous active power in each phase unit is derived in [14], considering negative-sequence circulating current. Under unbalanced conditions, however, positive- and zero-sequence components also exist in circulating current, making the derivation inaccurate. Additionally, the variation of circulating current components and the dc voltage/current ripple with different current control schemes remain unknown. Recently, according to ac/dc decomposed circuit of a single-phase MMC and active power balance between ac and dc terminals, a simple method is used for arm and circulating current calculation in [15]. Nevertheless, the dc voltage is assumed to be constant in this paper, while the real one under unbalance grid conditions contains double-line frequency ripple, which is also related with the unknown variables, i.e., circulating current, making the derivation invalid. Besides, neglecting the arm inductors and SM capacitors during the circulating current estimation, their impact cannot be revealed.

To the best knowledge of the authors, analytical description of an MMC under unbalanced conditions, including steady-state voltage, current quantities, and their interaction, has so far been missing. To fill this void and supply a theoretical approach for converter performance evaluation, this paper presents explicit analytical expressions for steady-state current and voltage quantities in an MMC under unbalanced grid conditions. Specifically, six equations for positive-, negative-, and zero-sequence double-line frequency circulating current can be derived based on the circular interaction of electrical quantities. By solving these equations, the circulating current components are obtained. Then, the fundamental and low-order harmonic components of the arm currents, capacitor charging currents,

---

Manuscript received April 10, 2016; revised July 9, 2016 and September 14, 2016; accepted November 7, 2016. Date of publication November 16, 2016; date of current version April 24, 2017. This work was supported primarily by the Engineering Research Center Program of the National Science Foundation and the Department of Energy under NSF Award Number EEC-1041877, and by the CURENT Industry Partnership Program. Recommended for publication by Associate Editor M. Hagiwara. *(Corresponding author: Xiaojie Shi).*

The authors are with the Center for Ultra-Wide-Area Resilient Electric Energy Transmission Networks, Department of Electrical Engineering and Computer Science, University of Tennessee, Knoxville, TN 37996-2250 USA (e-mail: xshi5@vols.utk.edu; ee.zqwang@gmail.com; bliu16@utk.edu; yli81@utk.edu; tolbert@utk.edu; fred.wang@utk.edu).

Color versions of one or more of the figures in this paper are available online at http://ieeexplore.ieee.org.

Digital Object Identifier 10.1109/TPEL.2016.2629472

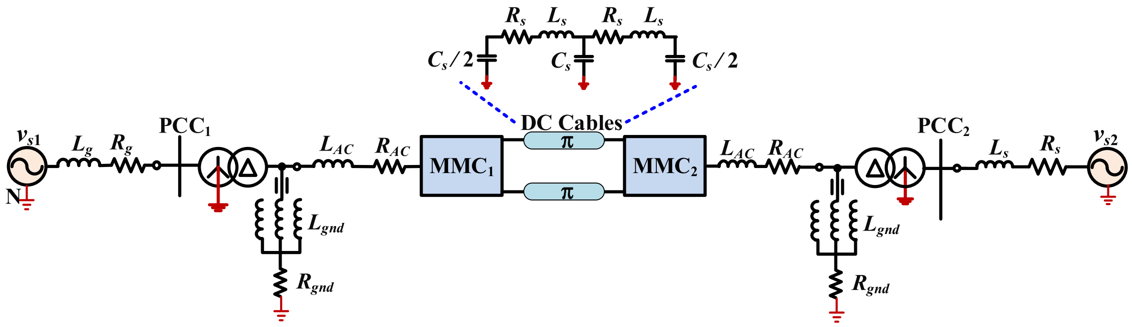

Fig. 1. Single-line diagram of an MMC-HVdc transmission system.

capacitor voltages, and ac-side phase voltages of MMC can also be calculated. With the steady-state model, the impact of negative-sequence current control on second-order current and voltage ripple is investigated. Furthermore, in order to predict the zero-sequence circulating current in a point-to-point HVdc system, the equivalent dc impedance of an MMC inverter is derived with/without the circulating current control.

The analytical expressions for circulating current, capacitor voltage, and associated variables can supply additional selection criteria for semiconductor devices and passive components, e.g., arm inductance and SM capacitance, suffering unbalanced operations. It also gives an insight into the impact of different control schemes on the fault characteristics and improves the understanding of the operation of an MMC under unbalanced conditions. Moreover, based on the inner relationship among voltage and current quantities, the derived equivalent dc impedance can be employed for both steady-state analysis and stability evaluation.

This paper is structured as follows: Section II briefly introduces the configuration of an MMC-based HVdc (MMC-HVdc) transmission system and the widely used dual-current control scheme with unbalanced ac grids. The interaction between voltage and current quantities is derived in Section III, and the impact of negative-sequence current control on system performance is also discussed. Section IV presents the circulating current calculation of an MMC rectifier with resistive and inverter loads. Experimental results obtained from a scaled-down three-phase MMC prototype are compared with the calculation results in Section V to validate the theoretical analysis and derived model. Section VI provides the conclusion for this paper.

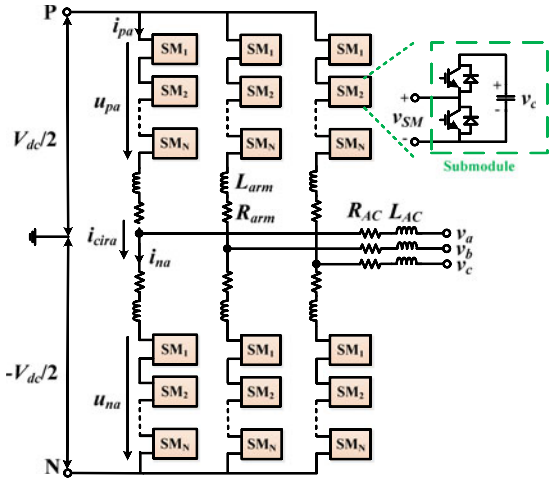

Fig. 2. Circuit configuration of an MMC.

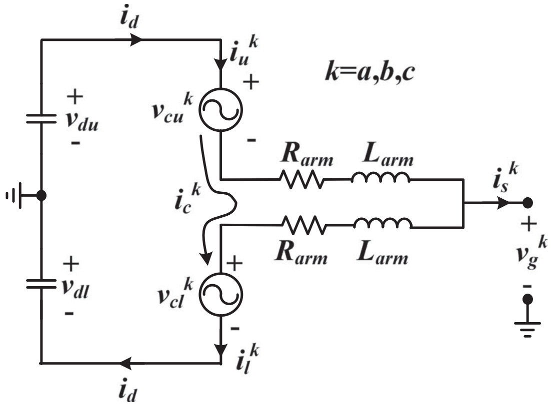

Fig. 3. Single-phase equivalent circuit of the MMC.

II. System Configuration and Control Schemes Under Unbalanced Conditions

Fig. 1 illustrates the single-line diagram of a typical point-to-point MMC-HVdc transmission system, where v_{s1} and v_{s2} represent ac grid voltages; L_g and R_g represent grid impedance; L_{AC} and R_{AC} are ac reactor and its equivalent parasitic resistance; R_s, L_s, and C_s are parasitic resistance, inductance, and capacitance of dc cables, respectively. For isolation and voltage conversion, the ac terminal of each MMC is connected to the grid voltage v_{s1} or v_{s2} through a three-phase Y/Δ transformer. It should be mentioned that other transformer structures can also be employed according to the commissioned MMC-HVdc systems [16], [17], but in order to block zero-sequence currents flowing between ac system and VSC unit, and maximize the output voltage capability of the converter by using SVM or third-harmonic voltage injection, a Y/Δ transformer is adopted in this paper [18]–[20]. Both converters are high resistance grounded at shunt reactor neutral points, and the two MMCs are connected through dc cables.

The configuration of an MMC is shown in Fig. 2. Each phase leg of the MMC consists of one upper and one lower arm connected in series between the dc terminals. N series-connected SMs and one-arm inductor L_{arm} form an arm. Each SM contains an IGBT half bridge as a switching element and a dc storage capacitor.

Fig. 3 illustrates the single-phase equivalent circuit of an MMC [21], where v_{du} and v_{dl} are the positive (upper) and

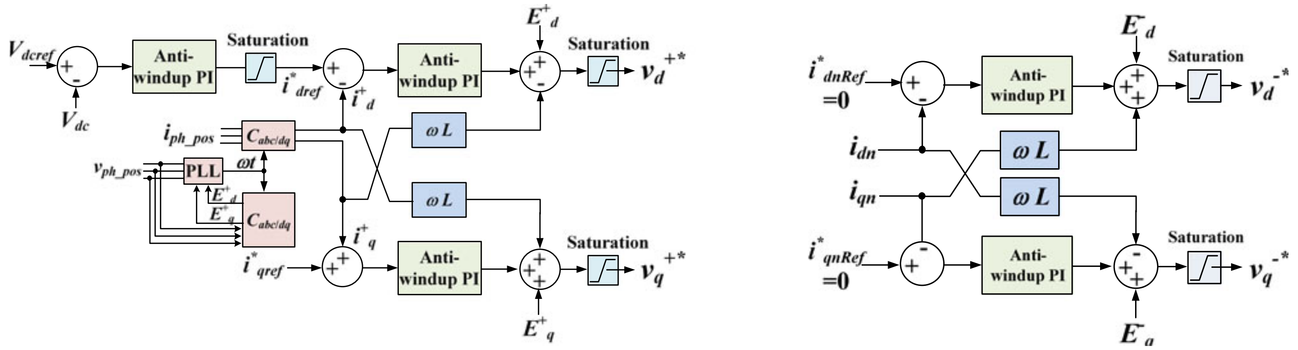

(a) (b)

Fig. 4. Diagram of dual-current control. (a) Positive-sequence current control. (b) Negative-sequence current suppression.

negative (lower) dc bus to ground voltage; i_d is the dc current; v_g^k and i_s^k represent the phase voltage and line current of phase *k*; v_{cu}^k and v_{cl}^k are the voltages produced by the SMs in the upper and lower arm, respectively; i_u^k and i_l^k denote the corresponding arm currents; and i_c^k is circulating current in phase *k*. The subscript "*u*" and "*l*" represent the upper and lower arm, respectively.

Fig. 4 shows the diagram of the classic dual-current control, which consists of positive- and negative-sequence current control [22], [23]. To achieve an accurate synchronization with the grid voltage, the positive-sequence voltage is extracted with methods proposed in [24] and used as the input of a phase-locked loop (PLL). Through park transformation and the angle locked by PLL, the converter-side phase current can be decomposed into positive- and negative-sequence components and regulated separately in *dq* coordinates. With accurate extraction of positive-, negative-, and zero-sequence voltage and current, as well as properly designed PI controllers, the negative-sequence phase current can be eliminated under unbalanced conditions. With Y/Δ transformers assumed in the studied MMC-HVdc system in this paper as shown in Fig. 1, zero-sequence current will be blocked under unbalanced grid conditions, and no corresponding current control is required [25].

III. STEADY-STATE MODEL FOR SECOND-ORDER PHASE VOLTAGE RIPPLE PREDICTION

A. Without Negative-Sequence Current Control

Assume a single-line-to-ground (SLG) fault occurring in the primary side of the Y/Δ transformer in MMC_1 station, which will create an unbalanced voltage in PCC_1 [26]–[29]. In this paper, SLG fault is used as a severe unbalanced case, which could last for certain time (normally 0.5 s) if single-pole switching (SPS) is adopted [30]–[32]. Within 0.5 s, the system can achieve steady state, making the steading state modeling applicable in this case.

Contributed by the delta connection of the interfacing transformer, no zero-sequence phase current will be induced in the converter side by the SLG fault. Moreover, the grounding impedance is assumed to be high enough to have a negligible zero-sequence grounding current, no matter whether SVM (or equivalent modulation scheme by injecting third harmonics) or SPWM is adopted, thus enabling low power losses, high utilization of dc voltage, and slight interference with SLG fault protection.

With all these assumptions, zero-sequence phase current is regarded as zero, and upper as well as lower arm current can be expressed in (1). If interfacing transformers without the delta connected winding and/or low impedance grounding scheme are adopted, zero-sequence component will be induced in the phase current. In this case, (1) should be modified accordingly to make the circulating current prediction more accurate

$$\begin{aligned} i_{au}(t) &= \frac{\sqrt{2}}{2}I^+\sin(\omega_1 t+\varphi_+)+\frac{\sqrt{2}}{2}I^-\sin(\omega_1 t+\varphi_-)\\ &\quad + I_{\mathrm{cda}} + I_c^+\sin(2\omega_1 t+\theta_+)+I_c^-\sin(2\omega_1 t+\theta_-)\\ &\quad + I_c^0\sin(2\omega_1 t+\theta_0)\\ i_{al}(t) &= -\frac{\sqrt{2}}{2}I^+\sin(\omega_1 t+\varphi_+)-\frac{\sqrt{2}}{2}I^-\sin(\omega_1 t+\varphi_-)\\ &\quad + I_{\mathrm{cda}} + I_c^+\sin(2\omega_1 t+\theta_+)+I_c^-\sin(2\omega_1 t+\theta_-)\\ &\quad + I_c^0\sin(2\omega_1 t+\theta_0) \end{aligned} \tag{1}$$

where I^+, I^- are the amplitudes of the positive- and negative-sequence phase current, respectively; φ_+, φ_- are the corresponding initial phase angles; I_{cda} represents the dc component in arm currents of phase A; ω_1 represents the fundamental frequency angular frequency; I_c^+, I_c^-, and I_c^0 denote the positive-, negative-, and zero-sequence circulating current, respectively, and θ_+, θ_-, and θ_0 are the corresponding initial phase angles. For simplicity, only the dominant second-order harmonics are considered in this paper.

According to the classic power system analysis theory under asymmetrical faults, phase voltages in the secondary side of Y/Δ transformer (v_A, v_B, v_c) can be calculated based on fault time, grid short-circuit capacity, and grounding impedance, either through offline evaluation or online computation [33]. Then, the phase voltage can be decomposed into positive- (v_{gj+}), negative- (v_{gj-}), and zero- (v_{gj0})sequence components [34]. When the negative-sequence current control is not used, ideally $v_{cj-}=0$, and the negative-sequence current can be calculated as $i_{j-}=\frac{v_{gj-}}{R_{\mathrm{AC}}+j\omega L_{\mathrm{AC}}}$.

Therefore, under certain operation conditions, I^+, I^-, φ_+, and φ_- in (1) can be regarded as known parameters based on power system fault calculation [35], [36], while I_c^+, I_c^-, I_c^0,

θ_+, θ_-, and θ_0 are unknown variables and will be calculated in the following derivation.

In practice, the equivalent switching frequency of MMC (Nf_c, f_c is the carrier frequency) is high enough to acquire a negligible high-frequency component in the switching functions. Therefore, an average switching function shown in (2) can be adopted in this analysis

$$\begin{aligned} S_{au\_av}\left(t\right) &= \frac{1}{2}\left[1 - M\sin\left(\omega_1 t\right)\right] \\ S_{al\_av}\left(t\right) &= \frac{1}{2}\left[1 + M\sin\left(\omega_1 t\right)\right] \end{aligned} \tag{2}$$

where *M* represents positive-sequence modulation index; $S_{au\_\mathrm{av}}\left(t\right)$ and $S_{al\_\mathrm{av}}\left(t\right)$ are average switching functions of the SMs in the upper and lower arms, respectively.

Based on (1) and (2), the associated current and voltage quantities can be expressed as follows:

1) Capacitor Charging Current: According to [37], the average capacitor charging current in the upper (i_{c_u}) and lower arm (i_{c_l}) can be expressed as

$$\begin{aligned} i_{c\_u}(t) = S_{au\_av}(t)\cdot i_{au}(t) = {} & \frac{1}{2}I_{\mathrm{cda}} - \frac{\sqrt{2}}{8}MI^+\cos\varphi_+ \\ & - \frac{\sqrt{2}}{8}MI^-\cos\varphi_- - \frac{1}{2}MI_{\mathrm{cda}}\sin(\omega_1 t) \\ & + \frac{\sqrt{2}}{4}I^+\sin(\omega_1 t + \varphi_+) + \frac{\sqrt{2}}{4}I^-\sin(\omega_1 t + \varphi_-) \\ & - \frac{1}{4}MI_C^+\cos(\omega_1 t + \theta_+) - \frac{1}{4}MI_C^-\cos(\omega_1 t + \theta_-) \\ & - \frac{1}{4}MI_C^0\cos(\omega_1 t + \theta_0) + \frac{\sqrt{2}}{8}MI^+\cos(2\omega_1 t + \varphi_+) \\ & + \frac{\sqrt{2}}{8}MI^-\cos(2\omega_1 t + \varphi_-) + \frac{1}{2}I_c^+\sin(2\omega_1 t + \theta_+) \\ & + \frac{1}{2}I_c^-\sin(2\omega_1 t + \theta_-) + \frac{1}{2}I_c^0\sin(2\omega_1 t + \theta_0) \\ & + \frac{1}{4}MI_c^+\sin(3\omega_1 t + \theta_+) + \frac{1}{4}MI_c^-\sin(3\omega_1 t + \theta_-) \\ & + \frac{1}{4}MI_c^0\sin(3\omega_1 t + \theta_0) \end{aligned}$$

$$\begin{aligned} i_{c\_l}(t) = S_{al\_av}(t)\cdot i_{al}(t) = {} & \frac{1}{2}I_{\mathrm{cda}} - \frac{\sqrt{2}}{8}MI^+\cos\varphi_+ \\ & - \frac{\sqrt{2}}{8}MI^-\cos\varphi_- + \frac{1}{2}MI_{\mathrm{cda}}\sin(\omega_1 t) \\ & - \frac{\sqrt{2}}{4}I^+\sin(\omega_1 t + \varphi_+) - \frac{\sqrt{2}}{4}I^-\sin(\omega_1 t + \varphi_-) \\ & + \frac{1}{4}MI_C^+\cos(\omega_1 t + \theta_+) + \frac{1}{4}MI_c^-\cos(\omega_1 t + \theta_-) \\ & + \frac{1}{4}MI_c^0\cos(\omega_1 t + \theta_0) + \frac{\sqrt{2}}{8}MI^+\cos(2\omega_1 t + \varphi_+) \\ & + \frac{\sqrt{2}}{8}MI^-\cos(2\omega_1 t + \theta_-) + \frac{1}{2}I_c^+\sin(2\omega_1 t + \theta_+) \\ & + \frac{1}{2}I_c^-\sin(2\omega_1 t + \theta_-) + \frac{1}{2}I_c^0\sin(2\omega_1 t + \theta_0) \\ & - \frac{1}{4}MI_c^+\sin(3\omega_1 t + \theta_+) - \frac{1}{4}MI_c^-\sin(3\omega_1 t + \theta_-) \\ & - \frac{1}{4}MI_c^0\sin(3\omega_1 t + \theta_0). \end{aligned} \tag{3}$$

The dc component highlighted by pink color in (3) is zero during steady state, which stands for a balanced active power between the ac and dc side. Solving the steady-state equation in (4) yields the dc component in circulating current

$$\begin{aligned} &\frac{1}{2}I_{\mathrm{cda}} - \frac{\sqrt{2}}{8}MI^+\cos\varphi_+ - \frac{\sqrt{2}}{8}MI^-\cos\varphi_- = 0 \rightarrow I_{\mathrm{cda}} \\ &= \frac{\sqrt{2}}{4}MI^+\cos\varphi_+ + \frac{\sqrt{2}}{4}MI^-\cos\varphi_- \end{aligned} \tag{4a}$$

$$\begin{aligned} &\frac{1}{2}I_{cdb} - \frac{\sqrt{2}}{8}MI^+\cos\varphi_+ - \frac{\sqrt{2}}{8}MI^-\cos(\varphi_- - 120^\circ) \\ &= 0 \rightarrow I_{cdb} = \frac{\sqrt{2}}{4}MI^+\cos\varphi_+ + \frac{\sqrt{2}}{4}MI^-\cos(\varphi_- - 120^\circ) \end{aligned} \tag{4b}$$

$$\begin{aligned} &\frac{1}{2}I_{cdc} - \frac{\sqrt{2}}{8}MI^+\cos\varphi_+ - \frac{\sqrt{2}}{8}MI^-\cos(\varphi_- + 120^\circ) \\ &= 0 \rightarrow I_{cdc} = \frac{\sqrt{2}}{4}MI^+\cos\varphi_+ + \frac{\sqrt{2}}{4}MI^-\cos(\varphi_- + 120^\circ). \end{aligned} \tag{4c}$$

Comparing (4a), (4b), and (4c), the dc components in the three-phase arm current are no longer equal to $I_{\mathrm{dc}}/3$ (which is $\sqrt{2}MI^+\cos\varphi_+/4$ in normal operation) under unbalanced conditions, indicating uneven active power contribution among three phases. Moreover, such asymmetrical distribution will be more severe with higher negative-sequence current I^-. Therefore, I_{cdk} ($k = \mathrm{a, b, c}$) in (1) should be replaced by (4) during the following derivation.

2) Capacitor Ripple Voltage: Multiplying the capacitor reactance $1/(j\omega_1 C_{\mathrm{sub}})$ and the fundamental frequency capacitor charging current in (3), the fundamental frequency capacitor ripple voltages in the upper and lower arms in phase A are obtained

$$\begin{aligned} u_{cu}^{(1)}\left(t\right) = \frac{1}{j\omega_1 C_{\mathrm{sub}}}i_{c\_u}^{(1)} = {} & \frac{MI_{\mathrm{cda}}}{2\omega_1 C_{\mathrm{sub}}}\cos\left(\omega_1 t\right) \\ & - \frac{\sqrt{2}}{4\omega_1 C_{\mathrm{sub}}}I^+\cos(\omega_1 t + \varphi_+) \\ & - \frac{\sqrt{2}}{4\omega_1 C_{\mathrm{sub}}}I^-\cos(\omega_1 t + \varphi_-) \\ & - \frac{1}{4\omega_1 C_{\mathrm{sub}}}MI_c^+\sin(\omega_1 t + \theta_+) \\ & - \frac{1}{4\omega_1 C_{\mathrm{sub}}}MI_c^-\sin(\omega_1 t + \theta_-) \\ & - \frac{1}{4\omega_1 C_{\mathrm{sub}}}MI_c^0\sin(\omega_1 t + \theta_0) \end{aligned}$$

$$\begin{aligned} u_{cl}^{(1)}(t) &= \frac{1}{j\omega_1 C_{\text{sub}}} i_{c\_l}^{(1)} = -\frac{MI_{\text{cda}}}{2\omega_1 C_{\text{sub}}}\cos(\omega_1 t) \\ &\quad + \frac{\sqrt{2}}{4\omega_1 C_{\text{sub}}} I^{+}\cos(\omega_1 t+\varphi_{+}) \\ &\quad + \frac{\sqrt{2}}{4\omega_1 C_{\text{sub}}} I^{-}\cos(\omega_1 t+\varphi_{-}) \\ &\quad + \frac{1}{4\omega_1 C_{\text{sub}}} MI_c^{+}\sin(\omega_1 t+\theta_{+}) \\ &\quad + \frac{1}{4\omega_1 C_{\text{sub}}} MI_c^{-}\sin(\omega_1 t+\theta_{-}) \\ &\quad + \frac{1}{4\omega_1 C_{\text{sub}}} MI_c^{0}\sin(\omega_1 t+\theta_{0}). \end{aligned} \tag{5}$$

$$\begin{aligned} u_{cu}^{(2)}(t) &= \frac{1}{j2\omega_1 C_{\text{sub}}} i_{c\_u}^{(2)} = \frac{\sqrt{2}MI^{+}}{16\omega_1 C_{\text{sub}}}\sin(2\omega_1 t+\varphi_{+}) \\ &+ \frac{\sqrt{2}MI^{-}}{16\omega_1 C_{\text{sub}}}\sin(2\omega_1 t+\varphi_{-}) - \frac{I_c^{+}}{4\omega_1 C_{\text{sub}}}\cos(2\omega_1 t+\theta_{+}) \\ &- \frac{I_c^{-}}{4\omega_1 C_{\text{sub}}}\cos(2\omega_1 t+\theta_{-}) - \frac{I_c^{0}}{4\omega_1 C_{\text{sub}}}\cos(2\omega_1 t+\theta_{0}) \\ u_{cl}^{(2)}(t) &= \frac{1}{j2\omega_1 C_{\text{sub}}} i_{c\_l}^{(2)} = \frac{\sqrt{2}MI^{+}}{16\omega_1 C_{\text{sub}}}\sin(2\omega_1 t+\varphi_{+}) \\ &+ \frac{\sqrt{2}MI^{-}}{16\omega_1 C_{\text{sub}}}\sin(2\omega_1 t+\varphi_{-}) - \frac{I_c^{+}}{4\omega_1 C_{\text{sub}}}\cos(2\omega_1 t+\theta_{+}) \\ &- \frac{I_c^{-}}{4\omega_1 C_{\text{sub}}}\cos(2\omega_1 t+\theta_{-}) - \frac{I_c^{0}}{4\omega_1 C_{\text{sub}}}\cos(2\omega_1 t+\theta_{0}) \end{aligned} \tag{6}$$

$$\begin{aligned} u_{cu}^{(3)}(t) &= \frac{1}{j3\omega_1 C_{\text{sub}}} i_{c_u}^{(3)} = \frac{MI_c^{+}}{12\omega_1 C_{\text{sub}}}\cos(3\omega_1 t+\theta_{+}) \\ &+ \frac{MI_c^{-}}{12\omega_1 C_{\text{sub}}}\cos(3\omega_1 t+\theta_{-}) + \frac{MI_c^{0}}{12\omega_1 C_{\text{sub}}}\cos(3\omega_1 t+\theta_{0}) \\ u_{cl}^{(3)}(t) &= \frac{1}{j3\omega_1 C_{\text{sub}}} i_{c_l}^{(3)} = -\frac{MI_c^{+}}{12\omega_1 C_{\text{sub}}}\cos(3\omega_1 t+\theta_{+}) \\ &- \frac{MI_c^{-}}{12\omega_1 C_{\text{sub}}}\cos(3\omega_1 t+\theta_{-}) - \frac{MI_c^{0}}{12\omega_1 C_{\text{sub}}}\cos(3\omega_1 t+\theta_{0}). \end{aligned} \tag{7}$$

3) Phase voltage ripple: The ac-side phase voltage ripples contributed by $u_{cu}^{(1)}$ and $u_{cl}^{(1)}$ can be expressed as

$$\begin{aligned} u_{ph\_1}(t) &= \frac{N}{2}\left[1-M\sin(\omega_1 t)\right]\cdot u_{cu}^{(1)}(t) \\ &+ \frac{N}{2}\left[1+M\sin(\omega_1 t)\right]\cdot u_{cl}^{(1)}(t) \\ &= -\frac{\sqrt{2}NMI^{+}}{8\omega_1 C_{\text{sub}}}\sin\varphi_{+} - \frac{\sqrt{2}NMI^{-}}{8\omega_1 C_{\text{sub}}}\sin\varphi_{-} \\ &+ \frac{NM^2 I_c^{+}}{8\omega_1 C_{\text{sub}}}\cos\theta_{+} + \frac{NM^2 I_c^{-}}{8\omega_1 C_{\text{sub}}}\cos\theta_{-} + \frac{NM^2 I_c^{0}}{8\omega_1 C_{\text{sub}}}\cos\theta_{0} \\ &- \frac{NM^2 I_{\text{cda}}}{4\omega_1 C_{sub}}\sin(2\omega_1 t) + \frac{\sqrt{2}NMI^{+}}{8\omega_1 C_{\text{sub}}}\sin(2\omega_1 t+\varphi_{+}) \\ &+ \frac{\sqrt{2}NMI^{-}}{8\omega_1 C_{\text{sub}}}\sin(2\omega_1 t+\varphi_{-}) - \frac{NM^2 I_c^{+}}{8\omega_1 C_{\text{sub}}}\cos(2\omega_1 t+\theta_{+}) \\ &- \frac{NM^2 I_c^{-}}{8\omega_1 C_{\text{sub}}}\cos(2\omega_1 t+\theta_{-}) - \frac{NM^2 I_c^{0}}{8\omega_1 C_{\text{sub}}}\cos(2\omega_1 t+\theta_{0}). \end{aligned} \tag{8a}$$

Phase voltage ripple contributed by $u_{cu,l}^{(2)}$ and $u_{cu,l}^{(3)}$ can be calculated as

$$\begin{aligned} u_{ph\_2}(t) &= \frac{N}{2}\left[1-M\sin(\omega_1 t)\right]\cdot u_{cu}^{(2)}(t) \\ &+ \frac{N}{2}\left[1+M\sin(\omega_1 t)\right]\cdot u_{cl}^{(2)}(t) \\ &= \frac{\sqrt{2}NMI^{+}}{16\omega_1 C_{\text{sub}}}\sin(2\omega_1 t+\varphi_{+}) + \frac{\sqrt{2}NMI^{-}}{16\omega_1 C_{\text{sub}}}\sin(2\omega_1 t+\varphi_{-}) \\ &- \frac{NI_c^{+}}{4\omega_1 C_{\text{sub}}}\cos(2\omega_1 t+\theta_{+}) - \frac{NI_c^{-}}{4\omega_1 C_{\text{sub}}}\cos(2\omega_1 t+\theta_{-}) \\ &- \frac{NI_c^{0}}{4\omega_1 C_{\text{sub}}}\cos(2\omega_1 t+\theta_{0}) \end{aligned} \tag{8b}$$

$$\begin{aligned} u_{ph\_3}(t) &= \frac{N}{2}\left[1-M\sin(\omega_1 t)\right]\cdot u_{cu}^{(3)}(t) \\ &+ \frac{N}{2}\left[1+M\sin(\omega_1 t)\right]\cdot u_{cl}^{(3)}(t) \\ &= -\frac{NM^2 I_c^{+}}{24\omega_1 C_{\text{sub}}}\cos(2\omega_1 t+\theta_{+}) - \frac{NM^2 I_c^{-}}{24\omega_1 C_{\text{sub}}}\cos(2\omega_1 t+\theta_{-}) \\ &- \frac{NM^2 I_c^{0}}{24\omega_1 C_{\text{sub}}}\cos(2\omega_1 t+\theta_{0}) + \frac{NM^2 I_c^{+}}{24\omega_1 C_{\text{sub}}}\cos(4\omega_1 t+\theta_{+}) \\ &+ \frac{NM^2 I_c^{-}}{24\omega_1 C_{\text{sub}}}\cos(4\omega_1 t+\theta_{-}) + \frac{NM^2 I_c^{0}}{24\omega_1 C_{\text{sub}}}\cos(4\omega_1 t+\theta_{0}). \end{aligned} \tag{8c}$$

As shown in (8), with arm current assumed in (1), the second- and fourth-order phase voltage components are generated, which in turn will create circulating current with the corresponding frequencies. Focusing on the dominant second-order ripples and ignoring the fourth-order items, the double-line frequency phase voltage ripple in Phase A can be obtained by summing all the second-order components in (8)

$$\begin{aligned} u_{ph\_A}^{(2)}(t) &= -\frac{\sqrt{2}NM^3 I^{+}}{16\omega_1 C_{\text{sub}}}\cos\varphi_{+}\sin(2\omega_1 t) \\ &+ \frac{3\sqrt{2}NMI^{+}}{16\omega_1 C_{\text{sub}}}\sin(2\omega_1 t+\varphi_{+}) - \frac{NM^2 I_c^{-}}{6\omega_1 C_{\text{sub}}}\cos(2\omega_1 t+\theta_{-}) \\ &- \frac{NI_c^{-}}{4\omega_1 C_{\text{sub}}}\cos(2\omega_1 t+\theta_{-}) - \frac{\sqrt{2}NM^3 I^{-}}{32\omega_1 C_{\text{sub}}}\sin(2\omega_1 t+\varphi_{-}) \\ &+ \frac{3\sqrt{2}NMI^{-}}{16\omega_1 C_{\text{sub}}}\sin(2\omega_1 t+\varphi_{-}) - \frac{NM^2 I_c^{0}}{6\omega_1 C_{\text{sub}}}\cos(2\omega_1 t+\theta_{0}) \\ &- \frac{NI_c^{0}}{4\omega_1 C_{\text{sub}}}\cos(2\omega_1 t+\theta_{0}) - \frac{\sqrt{2}NM^3 I^{-}}{32\omega_1 C_{\text{sub}}}\sin(2\omega_1 t-\varphi_{-}) \\ &- \frac{NM^2 I_c^{+}}{6\omega_1 C_{\text{sub}}}\cos(2\omega_1 t+\theta_{+}) - \frac{NI_c^{+}}{4\omega_1 C_{\text{sub}}}\cos(2\omega_1 t+\theta_{+}). \end{aligned} \tag{9}$$

Similarly, the second-order voltage ripple in Phases B and C can be given in (10) and (11). The negative-, zero-, and positive-sequence voltage ripples are distinguished by blue, red, and black colors

$$\begin{aligned} u_{ph\_B}^{(2)}(t) = &-\frac{\sqrt{2}NM^3I^+}{16\omega_1 C_{\rm sub}}\cos\varphi_+\sin(2\omega_1 t+120^\circ)\\ &+\frac{3\sqrt{2}NMI^+}{16\omega_1 C_{\rm sub}}\sin(2\omega_1 t+\varphi_+ +120^\circ)\\ &-\frac{NM^2I_c^-}{6\omega_1 C_{\rm sub}}\cos(2\omega_1 t+\theta_- +120^\circ)\\ &-\frac{NI_c^-}{4\omega_1 C_{\rm sub}}\cos(2\omega_1 t+\theta_- +120^\circ)\\ &-\frac{\sqrt{2}NM^3I^-}{32\omega_1 C_{\rm sub}}\sin(2\omega_1 t+\varphi_-)\\ &+\frac{3\sqrt{2}NMI^-}{16\omega_1 C_{\rm sub}}\sin(2\omega_1 t+\varphi_-)\\ &-\frac{NM^2I_c^0}{6\omega_1 C_{\rm sub}}\cos(2\omega_1 t+\theta_0)\\ &-\frac{NI_c^0}{4\omega_1 C_{\rm sub}}\cos(2\omega_1 t+\theta_0)\\ &-\frac{\sqrt{2}NM^3I^-}{32\omega_1 C_{\rm sub}}\sin(2\omega_1 t-\varphi_- -120^\circ)\\ &-\frac{NM^2I_c^+}{6\omega_1 C_{\rm sub}}\cos(2\omega_1 t+\theta_+ -120^\circ)\\ &-\frac{NI_c^+}{4\omega_1 C_{\rm sub}}\cos(2\omega_1 t+\theta_+ -120^\circ). \end{aligned} \tag{10}$$

$$\begin{aligned} u_{ph\_C}^{(2)}(t) = &-\frac{\sqrt{2}NM^3I^+}{16\omega_1 C_{\rm sub}}\cos\varphi_+\sin(2\omega_1 t-120^\circ)\\ &+\frac{3\sqrt{2}NMI^+}{16\omega_1 C_{\rm sub}}\sin(2\omega_1 t+\varphi_+ -120^\circ)\\ &-\frac{NM^2I_c^-}{6\omega_1 C_{\rm sub}}\cos(2\omega_1 t+\theta_- -120^\circ)\\ &-\frac{NI_c^-}{4\omega_1 C_{\rm sub}}\cos(2\omega_1 t+\theta_- -120^\circ)\\ &-\frac{\sqrt{2}NM^3I^-}{32\omega_1 C_{\rm sub}}\sin(2\omega_1 t+\varphi_-)\\ &+\frac{3\sqrt{2}NMI^-}{16\omega_1 C_{\rm sub}}\sin(2\omega_1 t+\varphi_-)\\ &-\frac{NM^2I_c^0}{6\omega_1 C_{\rm sub}}\cos(2\omega_1 t+\theta_0)\\ &-\frac{NI_c^0}{4\omega_1 C_{\rm sub}}\cos(2\omega_1 t+\theta_0)\\ &-\frac{\sqrt{2}NM^3I^-}{32\omega_1 C_{\rm sub}}\sin(2\omega_1 t-\varphi_- +120^\circ)\\ &-\frac{NM^2I_c^+}{6\omega_1 C_{\rm sub}}\cos(2\omega_1 t+\theta_+ +120^\circ)\\ &-\frac{NI_c^+}{4\omega_1 C_{\rm sub}}\cos(2\omega_1 t+\theta_+ +120^\circ). \end{aligned} \tag{11}$$

As can be observed in (9)–(11), the positive- and zero-sequence voltage ripples only exist under unbalanced grid conditions, while the negative-sequence component exists as long as the positive-sequence modulation index *M* and phase current I^+ are nonzero. Sharing the same expression as that under normal conditions, the negative-sequence circulating current will not change much if MI^+ remains.

B. With Negative-Sequence Current Control

If dual-current control is used, the negative-sequence phase current can be eliminated, and thus, the arm current in phase A becomes

$$\begin{aligned} i_{au}(t) &= \frac{\sqrt{2}}{2}I^+\sin(\omega_1 t+\varphi_+)+I_{\rm cda}+I_c^+\sin(2\omega_1 t+\theta_+)\\ &\quad+I_c^-\sin(2\omega_1 t+\theta_-)+I_c^0\sin(2\omega_1 t+\theta_0)\\ i_{al}(t) &= -\frac{\sqrt{2}}{2}I^+\sin(\omega_1 t+\varphi_+)+I_{\rm cda}+I_c^+\sin(2\omega_1 t+\theta_+)\\ &\quad+I_c^-\sin(2\omega_1 t+\theta_-)+I_c^0\sin(2\omega_1 t+\theta_0). \end{aligned} \tag{12}$$

If the negative-sequence current control is adopted, the converter should generate the same negative-sequence voltage as the grid (i.e., $v_{cj-}=v_{gj-}$) in order to eliminate the negative-sequence current (i.e., $i_{j-}=0$). The corresponding modulation index is $M_j{}^- = \frac{v_{cj\_}}{K_{\rm conv}}$, where $K_{\rm conv} = \frac{V_{\rm dc}}{2}$ for SPWM modulation scheme, and $K_{\rm conv} = \frac{V_{\rm dc}}{\sqrt{3}}$ for SVM or its equivalent modulation schemes, where $V_{\rm dc}$ is dc-side voltage. Therefore, the average switching function can be described as

$$\begin{aligned} S_{au_{av}}(t) &= \frac{1}{2}[1-M^+\sin(\omega_1 t)-M^-\sin(\omega_1 t+\gamma_-)\\ S_{al\_av}(t) &= \frac{1}{2}[1+M^+\sin(\omega_1 t)+M^-\sin(\omega_1 t+\gamma_-) \end{aligned} \tag{13}$$

where M^+ denotes the positive-sequence modulation index; M^- and γ_- represent the negative-sequence modulation index and its initial phase angle; $S_{au\_{\rm av}}(t)$ and $S_{al\_{\rm av}}(t)$ are average switching functions of the SMs in the upper and lower arms, respectively.

Following the same derivation steps above, the steady-state dc component in three-phase arm currents are given as

$$\begin{aligned} &\frac{1}{2}I_{\rm cda}-\frac{\sqrt{2}}{8}M^+I^+\cos\varphi_+-\frac{\sqrt{2}}{8}M^-I^+\cos(\gamma_- -\varphi_+)=0\\ &\rightarrow I_{\rm cda}=\frac{\sqrt{2}}{4}M^+I^+\cos\varphi_+ +\frac{\sqrt{2}}{4}M^-I^+\cos(\gamma_- -\varphi_+)\\ &I_{cdb}=\frac{\sqrt{2}}{4}M^+I^+\cos\varphi_+ +\frac{\sqrt{2}}{4}M^-I^+\cos(\gamma_- -\varphi_+ -120^\circ)\\ &I_{cdc}=\frac{\sqrt{2}}{4}M^+I^+\cos\varphi_+ +\frac{\sqrt{2}}{4}M^-I^+\cos(\gamma_- -\varphi_+ +120^\circ). \end{aligned} \tag{14}$$

According to (14), the negative-sequence current control cannot equalize three-phase dc arm currents.

The double-line frequency ac voltage ripple in phase A is derived in (15), where the negative-, zero-, and positive-sequence circulating three-phase voltage ripples are still distinguished by blue, red, and black colors. The voltage ripple for Phase B and C can be obtained in the same manner, with a phase shift of $\pm 2\pi/3$ in negative- and positive-sequence components, and no phase shift for zero-sequence components (15) as shown at the bottom of this page.

As indicated in (15), with negative-sequence phase current control, more combinations of current and modulation index serve as the sources of double-line frequency phase voltage ripple. Moreover, compared to the result without negative-sequence current control in (9), the circulating current components in (15) are no longer decoupled. For example, I_c^+ and I_c^0 contribute to negative-sequence phase voltage ripple, and consequently are associated with I_c^-.

In summary, compared to [37], the steady-state model under unbalanced conditions is more complicated, especially when negative-sequence phase current control is adopted. The dc components in three-phase circulating current are no longer equal to each other and have a magnitude of $I_{\mathrm{dc}}/3$. In addition, the positive- as well zero-sequence circulating current will also be generated, which may require either passive components redesign, e.g., arm inductance and SM capacitance, or modification of the control scheme for effective circulating current suppression.

The above analytical expressions are derived based on the generic inner relationships among current and voltage quantities, which are applicable to MMC under both rectifier and inverter modes.

IV. STEADY-STATE MODEL FOR CIRCULATING CURRENT PREDICTION

With the derived steady-state model for second-order phase voltage ripple, the circulating current can be predicted by solving the equivalent circuit shown in Fig. 5(a) and (b), where $u^{+}_{ph_{-j}}$ and $u^{-}_{ph_{-j}}$ ($j = \mathrm{A, B, C}$) represent the corresponding three-phase double-line frequency voltage ripple in (9) and (15). The three-phase circulating current generated by the two voltage sources will add to zero and only circulate among phases. While for the zero-sequence circulating currents generated by $u^{0}_{ph_{-j}}$, they cannot cancel with each other and have to flow into the dc bus. Consequently, in addition to arm inductance L_{arm} and its ESR R_{arm}, the equivalent dc load impedance $Z_{\mathrm{dc\_eq}}$ will be incorporated into its equivalent circuit, as shown in Fig. 5(c).

Based on these equivalent circuits, the following equations hold

$$\begin{aligned}
i^{-}_{c\_k}(t) &= I_c^- \sin(2\omega_1 t + \theta_-) = -\frac{u^{-}_{ph\_k}(t)}{j2\omega_1 \cdot 2L_{\mathrm{arm}} + 2R_{\mathrm{arm}}} \\
i^{+}_{c\_k}(t) &= I_c^+ \sin(2\omega_1 t + \theta_+) = -\frac{u^{+}_{ph_k}(t)}{j2\omega_1 \cdot 2L_{\mathrm{arm}} + 2R_{\mathrm{arm}}} \\
&\qquad (k = \mathrm{A, B, C}) \\
i^{0}_{c\_k}(t) &= I_c^0 \sin(2\omega_1 t + \theta_0) \\
&= -\frac{u^{0}_{ph_k}(t)}{j2\omega_1 \cdot 2L_{\mathrm{arm}} + 2R_{\mathrm{arm}} + 3Z_{\mathrm{dc_{eq}}}(t)}.
\end{aligned} \tag{16}$$

From (16), circular interactions among double-line frequency voltages and currents in the MMC can be found. Moreover, by substituting (9) and (15) into (16) and solving the obtained equations, magnitudes (I_c^+, I_c^-, I_c^0) and initial phase angles

$$\begin{aligned}
u^{(2)}_{ph}(t) = &-\frac{\sqrt{2}N(M^+)^3 I^+}{16\omega_1 C_{\mathrm{sub}}}\cos\varphi_+ \sin(2\omega_1 t) - \frac{\sqrt{2}NM^+(M^-)^2 I^+}{16\omega_1 C_{\mathrm{sub}}}\sin(2\omega_1 t + \varphi_+) - \frac{\sqrt{2}N(M^-)^3 I^+}{32\omega_1 C_{\mathrm{sub}}}\sin(2\omega_1 t + 3\gamma_- - \varphi_+) \\
&+ \frac{3\sqrt{2}NM^+ I^+}{16\omega_1 C_{\mathrm{sub}}}\sin(2\omega_1 t + \varphi_+) - \frac{N(M^+)^2 I_c^-}{6\omega_1 C_{\mathrm{sub}}}\cos(2\omega_1 t + \theta_-) - \frac{N(M^-)^2 I_c^-}{6\omega_1 C_{\mathrm{sub}}}\cos(2\omega_1 t + \theta_-) \\
&- \frac{NM^+M^- I_c^0}{6\omega_1 C_{\mathrm{sub}}}\cos(2\omega_1 t + \theta_0 - \gamma_-) - \frac{NM^+M^- I_c^+}{6\omega_1 C_{\mathrm{sub}}}\cos(2\omega_1 t + \theta_+ + \gamma_-) - \frac{NI_c^-}{4\omega_1 C_{\mathrm{sub}}}\cos(2\omega_1 t + \theta_-) \\
&- \frac{\sqrt{2}NM^-(M^+)^2 I^+}{32\omega_1 C_{\mathrm{sub}}}\sin(2\omega_1 t + \gamma_- - \varphi_+) - \frac{\sqrt{2}NM^-(M^+)^2 I^+}{8\omega_1 C_{\mathrm{sub}}}\cos\varphi_+ \sin(2\omega_1 t + \gamma_-) \\
&- \frac{\sqrt{2}N(M^-)^3 I^+}{32\omega_1 C_{\mathrm{sub}}}\sin(2\omega_1 t + \gamma_- + \varphi_+) + \frac{3\sqrt{2}NM^- I^+}{16\omega_1 C_{\mathrm{sub}}}\sin(2\omega_1 t + \varphi_+ + \gamma_-) - \frac{N(M^+)^2 I_c^0}{6\omega_1 C_{\mathrm{sub}}}\cos(2\omega_1 t + \theta_0) \\
&- \frac{NI_c^0}{4\omega_1 C_{\mathrm{sub}}}\cos(2\omega_1 t + \theta_0) - \frac{NM^+M^- I_c^+}{6\omega_1 C_{\mathrm{sub}}}\cos(2\omega_1 t + \theta_+ - \gamma_-) - \frac{NM^+M^- I_c^-}{6\omega_1 C_{\mathrm{sub}}}\cos(2\omega_1 t + \theta_- + \gamma_-) \\
&- \frac{N(M^-)^2 I_c^0}{6\omega_1 C_{\mathrm{sub}}}\cos(2\omega_1 t + \theta_0) - \frac{\sqrt{2}NM^-(M^+)^2 I^+}{32\omega_1 C_{\mathrm{sub}}}\sin(2\omega_1 t + \varphi_+ - \gamma_-) - \frac{\sqrt{2}NM^+(M^-)^2 I^+}{16\omega_1 C_{\mathrm{sub}}}\sin(2\omega_1 t - \varphi_+ + 2\gamma_-) \\
&- \frac{\sqrt{2}NM^+(M^-)^2 I^+}{16\omega_1 C_{\mathrm{sub}}}\cos\varphi_+ \sin(2\omega_1 t + 2\gamma_-) - \frac{N(M^+)^2 I_c^+}{6\omega_1 C_{\mathrm{sub}}}\cos(2\omega_1 t + \theta_+) - \frac{NM^+M^- I_c^-}{6\omega_1 C_{\mathrm{sub}}}\cos(2\omega_1 t + \theta_- - \gamma_-) \\
&- \frac{NM^+M^- I_c^0}{6\omega_1 C_{\mathrm{sub}}}\cos(2\omega_1 t + \theta_0 + \gamma_-) - \frac{N(M^-)^2 I_c^+}{6\omega_1 C_{\mathrm{sub}}}\cos(2\omega_1 t + \theta_+) - \frac{NI_c^+}{4\omega_1 C_{\mathrm{sub}}}\cos(2\omega_1 t + \theta_+)
\end{aligned} \tag{15}$$

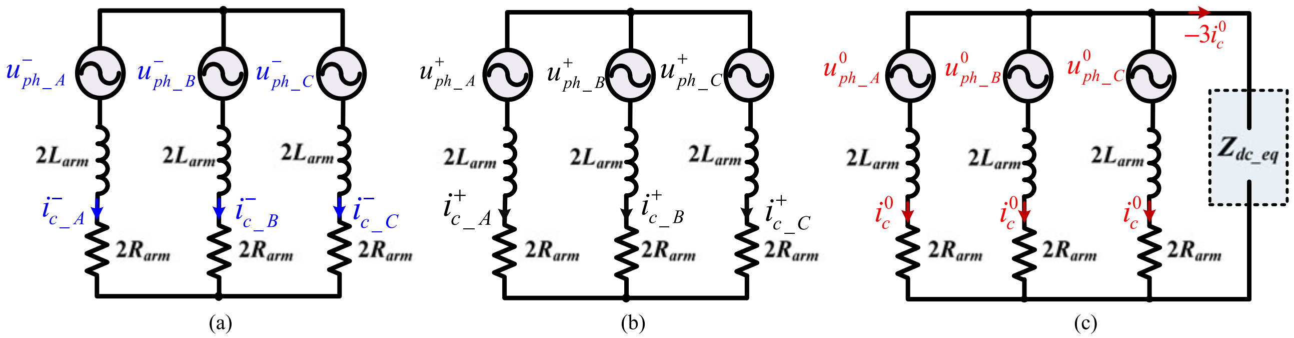

Fig. 5. Equivalent circuit of the circulating current. (a) Negative sequence. (b) Positive sequence. (c) Zero sequence.

(θ_+, θ_-, θ_0) of circulating current with and without negative-sequence current control can be calculated theoretically. With the calculated circulating current, all the previous equations will become explicit.

In the following part, the solving process of the circulating current is analyzed in two cases, i.e., an MMC rectifier with resistive load and inverter load (see MMC-HVdc in Fig. 1).

A. Resistive Load

1) Without Negative-Sequence Current Control: The corresponding equations with a dc-side resistive load R_L is given in (17), by replacing $Z_{\text{dc\_eq}}$ with R_L in (16). As mentioned earlier, the phase current amplitude I^+, I^-, phase angle φ_+, φ_-, and modulation index M are known variables. The magnitude and initial phase angle of different circulating current components ($I_c^+, I_c^-, I_c^0, \theta_+, \theta_-,$ and θ_0) can be easily calculated using (17). In addition, capacitor charging current, capacitor voltage ripple, and phase voltage ripple can be expressed by substituting the calculated circulating current components into (3)–(8).

$$\begin{aligned}
&(B-2A)\, I^+ \cos\varphi_+ = -EI_c^- \sin\theta_- - 2R_{\text{arm}} I_c^- \cos\theta_- \\
&BI^+ \sin\varphi_+ = EI_c^- \cos\theta_- - 2R_{\text{arm}} I_c^- \sin\theta_- \\
&(B-A)\, I^- \cos\varphi_- = -EI_c^0 \sin\theta_0 - (2R_{\text{arm}} + 3R_L) I_c^0 \cos\theta_0 \\
&(B-A)\, I^- \sin\varphi_- = EI_c^0 \cos\theta_0 - (2R_{\text{arm}} + 3R_L) I_c^0 \sin\theta_0 \\
&-AI^- \cos\varphi_- = -EI_c^+ \sin\theta_+ - 2R_{\text{arm}} I_c^+ \cos\theta_+ \\
&AI^- \sin\varphi_- = EI_c^+ \cos\theta_+ - 2R_{\text{arm}} I_c^+ \sin\theta_+
\end{aligned} \tag{17}$$

where,

$$A = \frac{\sqrt{2}NM^3}{32\omega_1 C_{\text{sub}}} \quad B = \frac{3\sqrt{2}NM}{16\omega_1 C_{\text{sub}}} \quad C = \frac{NM^2}{6\omega_1 C_{\text{sub}}}$$

$$D = \frac{N}{4\omega_1 C_{\text{sub}}} \quad E = C + D - 4\omega_1 L_{\text{arm}}.$$

Under slightly unbalanced conditions, the magnitude of negative-sequence circulating current keeps almost the same since I^+ and M will not change much. Nevertheless, if an SLG fault occurs, M will decrease because of the lost phase voltage, while I^+ tends to increase to maintain dc voltage and/or output power. Therefore, the negative-sequence circulating current will vary accordingly with different control schemes and current limit settings. As for the positive- and zero-sequence circulating current, their magnitudes are proportional to the negative-sequence phase current, and will reduce with lower M. Zero-sequence circulating current, limited by dc load impedance, will be much lower than the other two sequence components in an MMC rectifier with a light load.

According to (17), the variation of arm inductance and SM capacitance will also affect the magnitude and angle of circulating current, and thus, can be selected accordingly to meet a specific requirement under unbalanced conditions. In addition, a resonance point exists when $E = C + D - 4\omega_1 L_{\text{arm}} \;\; 0$, which leads to a huge circulating current and should be avoided to prevent power devices and passive components from damage.

2) With Negative-Sequence Current Control: By substituting (15) to (16) and replacing $Z_{\text{dc\_eq}}$ with R_L, the six equations used for circulating current calculation with a resistive load R_L

$$\begin{aligned}
&-2AI^+ \cos\varphi_+ - BI^+ \cos\varphi_+ - CI^+ \cos(3\gamma_- - \varphi_+) + DI^+ M^+ \cos\varphi_+ + GI_c^0 \sin(\theta_0 - \gamma_-) + GI_c^+ \sin(\theta_+ + \gamma_-) \\
&= -KI_c^- \sin\theta_- - 2R_{\text{arm}} I_c^- \cos\theta_- - BI^+ \sin\varphi_+ - CI^+ \sin(3\gamma_- - \varphi_+) + DI^+ M^+ \sin\varphi_+ - GI_c^0 \cos(\theta_0 - \gamma_-) \\
&-GI_c^+ \cos(\theta_+ + \gamma_-) = KI_c^- \cos\theta_- - 2R_{\text{arm}} I_c^- \sin\theta_- - PI^+ \cos(\gamma_- - \varphi_+) - 4PI^+ \cos\varphi_+ \cos\gamma_- \\
&-CI^+ \cos(\gamma_- + \varphi_+) + DI^+ M^- \cos(\gamma_- + \varphi_+) + GI_c^+ \sin(\theta_+ - \gamma_-) + GI_c^- \sin(\theta_- + \gamma_-) = -KI_c^0 \sin\theta_0 \\
&-(2R_{\text{arm}} + 3R_L) I_c^0 \cos\theta_0 - PI^+ \sin(\gamma_- - \varphi_+) - 4PI^+ \cos\varphi_+ \sin\gamma_- - CI^+ \sin(\gamma_- + \varphi_+) + DI^+ M^- \sin(\gamma_- + \varphi_+) \\
&-GI_c^+ \cos(\theta_+ - \gamma_-) - GI_c^- \cos(\theta_- + \gamma_-) = KI_c^0 \cos\theta_0 - (2R_{\text{arm}} + 3R_L) I_c^0 \sin\theta_0 - PI^+ \cos(\varphi_+ - \gamma_-) \\
&-BI^+ \cos(2\gamma_- - \varphi_+) - BI^+ \cos\varphi_+ \cos 2\gamma_- + GI_c^- \sin(\theta_- - \gamma_-) + GI_c^0 \sin(\theta_0 + \gamma_-) = -KI_c^+ \sin\theta_+ \\
&-2R_{\text{arm}} I_c^+ \cos\theta_+ - PI^+ \sin(\varphi_+ - \gamma_-) - BI^+ \sin(2\gamma_- - \varphi_+) - BI^+ \cos\varphi_+ \sin 2\gamma_- - GI_c^- \cos(\theta_- - \gamma_-) - \\
&GI_c^0 \cos(\theta_0 + \gamma_-) = KI_c^+ \cos\theta_+ - 2R_{\text{arm}} I_c^+ \sin\theta_+
\end{aligned} \tag{18}$$

are given in (18) as shown at the bottom of the previous page, when negative-sequence current control is activated
where,

$$A=\frac{\sqrt{2}N(M^{+})^{3}}{32\omega_1 C_{\mathrm{sub}}}\quad B=\frac{\sqrt{2}NM^{+}(M^{-})^{2}}{16\omega_1 C_{\mathrm{sub}}}\quad C=\frac{\sqrt{2}N(M^{-})^{3}}{32\omega_1 C_{\mathrm{sub}}}$$

$$D=\frac{3\sqrt{2}N}{16\omega_1 C_{\mathrm{sub}}}\quad E=\frac{N(M^{+})^{2}}{6\omega_1 C_{\mathrm{sub}}}\quad F=\frac{N(M^{-})^{2}}{6\omega_1 C_{\mathrm{sub}}}$$

$$G=\frac{NM^{+}M^{-}}{6\omega_1 C_{\mathrm{sub}}}H=\frac{N}{4\omega_1 C_{\mathrm{sub}}}$$

$$P=\frac{\sqrt{2}N(M^{+})^{2}M^{-}}{32\omega_1 C_{\mathrm{sub}}}K=E+F+H-4\omega_1 L_{\mathrm{arm}}.$$

Compared to (17), the elimination of negative-sequence current I^{-} does not remove the positive- and zero-sequence circulating current. In addition, they are generated not only by different combinations of positive-sequence current I^{+} and modulation index M^{+}, M^{-}, but also other circulating current components by a ratio of *G*. Due to such couplings, (18) becomes more difficult to solve, and the variation of circulating current magnitude and phase angles is not straightforward.

B. MMC Load

In a point-to-point MMC-HVdc system (see Fig. 1), an MMC inverter instead of a resistor serves as the dc load. According to Fig. 5, the equations for negative- and positive-sequence circulating currents in (17) and (18) keep the same, while the dc impedance $Z_{\mathrm{dc\_eq}}$ in Fig. 5(c) changes from R_L to the dc equivalent impedance of the MMC inverter.

In order to obtain the equivalent circuit of zero-sequence circulating current in an MMC-HVdc system, the dc equivalent impedance of the MMC inverter is derived as follows.

From the single-phase equivalent circuit in Fig. 3, one obtains

$$v_{du}-v_{cu}^{k}-R_{\mathrm{arm}}i_u^k-L_{\mathrm{arm}}\frac{di_u^k}{dt}=v_g^k \tag{19}$$

$$-v_{dl}+v_{cl}^{k}+R_{\mathrm{arm}}i_l^k+L_{\mathrm{arm}}\frac{di_l^k}{dt}=v_g^k. \tag{20}$$

Adding (19) and (20) yields

$$L_{\mathrm{arm}}\frac{di_u^k}{dt}+L_{\mathrm{arm}}\frac{di_l^k}{dt}+v_{cu}^k+v_{cl}^k+R_{\mathrm{arm}}i_u^k+R_{\mathrm{arm}}i_l^k=v_d \tag{21}$$

where v_d is the pole to pole dc bus voltage, and $v_d = v_{du} + v_{dl}$.

According to [38] and [39], v_{cu}^k and v_{cl}^k can be calculated as

$$v_{cu}^k=n_u^k v_{cu}^{\sum^k}\ v_{cl}^k=n_l^k v_{cl}^{\sum^k} \tag{22}$$

where n_u^k and n_l^k are insertion indices and $v_{cu,}^{\mathrm{k}}$ v_{cl}^{k} are the sum of capacitor voltages in phase *k* (*k* = *a*, *b*, *c*). In addition, n_u^k and n_l^k are given as

$$\begin{aligned}n_u^k&=\frac{v_{du}-v_s^{\mathrm{ref}k}-v_{\mathrm{cir}}^{\mathrm{ref}k}}{v_{cu}^{\sum k}}\approx\frac{v_{du}-v_s^{\mathrm{ref}k}-v_{\mathrm{cir}}^{\mathrm{ref}k}}{V_d}\\ n_l^k&=\frac{v_{dl}+v_s^{\mathrm{ref}k}-v_{\mathrm{cir}}^{\mathrm{ref}k}}{v_{cl}^{\sum k}}\approx\frac{v_{dl}+v_s^{\mathrm{ref}k}-v_{\mathrm{cir}}^{\mathrm{ref}k}}{V_d}\end{aligned} \tag{23}$$

where v_s^{refk} is the reference of the fundamental frequency output voltage and v_{cir}^{refk} is the reference generated by the circulating current control. An assumption is made here that the SM capacitance C_{sub} is selected to be large enough to guarantee that $v_{cu}^{\sum\mathrm{k}}\approx v_{cl}^{\sum\mathrm{k}}\approx V_d$ in each phase.

Substituting (23) into (22) yields

$$\begin{aligned}v_{cu}^k+v_{cl}^k&=\frac{v_{du}-v_s^{\mathrm{ref}k}-v_{\mathrm{cir}}^{\mathrm{ref}k}}{V_d}v_{cu}^{\sum k}+\frac{v_{dl}+v_s^{\mathrm{ref}k}-v_{\mathrm{cir}}^{\mathrm{ref}k}}{V_d}v_{cl}^{\sum k}\\ &=\frac{1}{2}v_c^{\sum k}-\frac{v_{\mathrm{cir}}^{\mathrm{ref}k}}{V_d}v_c^{\sum k}-\frac{v_s^{\mathrm{ref}k}}{V_d}v_c^{\Delta k}\end{aligned} \tag{24}$$

where $v_c^{\sum\mathrm{k}}$ is the total capacitor voltage in phase *k*, and $v_c^{\sum\mathrm{k}}=v_{cu}^{\sum\mathrm{k}}+v_{cl}^{\sum\mathrm{k}}$; v_c^{k} is the unbalance capacitor voltage in phase *k*, and $v_c^{\mathrm{k}}=v_{cu}^{\mathrm{k}}-v_{cl}^{\mathrm{k}}$.

Substituting (24) into (21) and adding the three-phase equations together yield

$$\begin{aligned}&L_{\mathrm{arm}}\frac{d}{dt}\sum_{k=1}^{3}i_u^k+L_{\mathrm{arm}}\frac{d}{dt}\sum_{k=1}^{3}i_l^k+\frac{1}{2}\sum_{k=1}^{3}v_c^{\sum k}\\ &\quad-\frac{1}{V_d}\sum_{k=1}^{3}v_{cir}^{refk}v_c^{\sum k}-\frac{1}{V_d}\sum_{k=1}^{3}v_s^{refk}v_c^{\Delta k}\\ &\quad+R_{\mathrm{arm}}\sum_{k=1}^{3}i_u^k+R_{\mathrm{arm}}\sum_{k=1}^{3}i_l^k=3v_d.\end{aligned} \tag{25}$$

As shown in Fig. 2, the summation of three-phase upper or lower arm currents is dc current, i.e.,

$$\sum_{k=1}^{3}i_u^k=\sum_{k=1}^{3}i_l^k=\sum_{k=1}^{3}i_c^k=i_d. \tag{26}$$

According to [38], the dynamics of an MMC can be described by the state variables v_c^{k} and v_c^{k}, as shown in (27) to (29). Moreover, v_c^{k} equals to $2V_d$ in the steady state, and v_c^{k} only contains fundamental frequency component

$$\frac{C_{\mathrm{sub}}}{N}\frac{dv_c^{\sum^k}}{dt}=-\frac{v_s^{\mathrm{ref}k}i_s^k}{V_d}+\left(1-\frac{2v_{\mathrm{cir}}^{\mathrm{ref}k}}{V_d}\right)i_c^k \tag{27}$$

$$\frac{C_{\mathrm{sub}}}{N}\frac{dv_c^{\Delta k}}{dt}=\left(1-\frac{2v_{\mathrm{cir}}^{\mathrm{ref}k}}{V_d}\right)\frac{i_s^k}{2}-\frac{2v_s^{\mathrm{ref}k}}{V_d}i_c^k \tag{28}$$

$$L_{\mathrm{arm}}\frac{di_c^k}{dt}=\frac{1}{2}\left(v_d-\frac{v_c^k}{2}+\frac{v_{\mathrm{cir}}^{\mathrm{ref}k}}{V_d}v_c^k+\frac{v_s^{\mathrm{ref}k}}{V_d}v_c^{\Delta k}\right)-R_{arm}i_c^k. \tag{29}$$

If v_s^{ref} and i_s in phase A are controlled as

$$v_s^{\mathrm{ref}}=V_s\cos(\omega_1 t)\quad i_s=I_s\cos(\omega_1 t-\varphi). \tag{30}$$

Equation (27) can be rewritten as

$$\begin{aligned}\frac{C_{\mathrm{sub}}}{N}\frac{dv_c^{\sum^k}}{dt}&=-\frac{V_sI_s\cos\varphi}{2V_d}-\frac{V_sI_s\cos(2\omega_1 t-\varphi)}{2V_d}\\ &\quad+\left(1-\frac{2v_{\mathrm{cir}}^{\mathrm{ref}k}}{V_d}\right)i_c^k.\end{aligned} \tag{31}$$

As can be observed, a second-order ripple is contained in v_c^{k}, and the dc component in the circulating current can be calculated as

$$I_{c0} = \frac{V_s I_s \cos\varphi}{2V_d}. \tag{32}$$

In the following derivation of dc-side equivalent impedance, two cases (with and without circulating current control) are considered.

1) Without Circulating Current Control: If no circulating current control is employed, i.e., $v_{\mathrm{cir}}^{refk} = 0$, the following equations hold:

$$\begin{aligned} &L_{\mathrm{arm}} \frac{d}{dt} \sum_{k=1}^{3} i_u^k + L_{\mathrm{arm}} \frac{d}{dt} \sum_{k=1}^{3} i_l^k + \frac{1}{2} \sum_{k=1}^{3} v_c^k \\ &- \frac{1}{V_d} \sum_{k=1}^{3} v_s^{refk} v_c^{\Delta k} + R_{\mathrm{arm}} \sum_{k=1}^{3} i_u^k + R_{\mathrm{arm}} \sum_{k=1}^{3} i_l^k = 3V_d \end{aligned} \tag{33}$$

$$\frac{C_{\mathrm{sub}}}{N} \frac{dv_c^{\sum k}}{dt} = -\frac{V_s I_s \cos\varphi}{2V_d} - \frac{V_s I_s \cos(2\omega_1 t - \varphi)}{2V_d} + i_c^k. \tag{34}$$

Therefore, the three phase summation of (34) yields

$$\frac{d}{dt} \sum_{k=1}^{3} v_c^k = \frac{N}{C_{\mathrm{sub}}} \left(-\frac{3V_s I_s \cos\varphi}{2V_d} + i_d \right). \tag{35}$$

For simplicity, the MMC system, including upper and lower arm impedance, is assumed to be symmetrical, and $v_c^{\mathrm{k}} = 0$, so no dc components will be generated by the product of v_s^{refk} and v_c^{k}, hence

$$\sum_{k=1}^{3} v_s^{\mathrm{ref}k} v_c^{\Delta k} = 0. \tag{36}$$

Substituting (26), (35), and (36) into (33) and applying linearization, one obtains

$$\begin{aligned} \tilde{v}_d &= \frac{2L_{\mathrm{arm}}}{3} \frac{d\tilde{i}_d}{dt} + \frac{N}{6C_{\mathrm{sub}}} \int^{\tilde{i}_d} + \frac{2R_{\mathrm{arm}}}{3} \tilde{i}_d \rightarrow \frac{\tilde{v}_d(s)}{\tilde{i}_d(s)} \\ &= \frac{2sL_{\mathrm{arm}}}{3} + \frac{N}{6sC_{\mathrm{sub}}} + \frac{2R_{\mathrm{arm}}}{3}. \end{aligned} \tag{37}$$

During the linearization procedure, no product of two small signal items is found at the second-harmonic frequency, and thus, the system has a linear characteristic for the double-line frequency voltage and current ripples. In addition, according to (37), if no circulating current control is used, an MMC inverter can be regarded as a series-connected *R–L–C* branch in the dc side. The parameters of this *R—L–C* branch are independent of implemented control schemes, and will remain with open-loop, current-loop, or power-loop regulation.

2) With Circulating Current Control: For simplicity, a proportional circulating current control applied in [39] is adopted, and

$$v_{\mathrm{cir}}^{\mathrm{ref}k} = R_a \left(i_c^{\mathrm{ref}} - i_c \right) + \hat{R} i_c^{\mathrm{ref}} \tag{38}$$

where $\hat{R}$ is an estimation of R_{arm}, and $\hat{R} i_c^{\mathrm{ref}}$ can be interpreted as a compensation of the voltage drop on R_{arm} in steady state. The circulating current reference is the same as I_{c0} in (32).

Substituting (38) into (31), applying linearization and disregarding the quasi-stationary components, one obtains

$$\frac{1}{2} \sum_{k=1}^{3} \tilde{v}_c^k = \frac{N}{2C_{\mathrm{sub}}} \left(1 + \frac{2(R_a - R_{arm}) I_{c0}}{V_d} \right) \int^{\tilde{i}_d}. \tag{39}$$

Substituting (38) into the fourth term of (25), the following equation holds:

$$\begin{aligned} \frac{1}{V_d} \sum_{k} &= 1^3 \tilde{v}_{\mathrm{cir}}^{\mathrm{ref}k} \tilde{v}_c^k = \frac{1}{V_d} \sum_{k=1}^{3} (-R_a \cdot 2V_d \tilde{i}_c^k \\ &\qquad + \frac{N}{C_{\mathrm{sub}}} R_{\mathrm{arm}} I_{c0} \cdot \left(1 + \frac{2(R_a - R_{\mathrm{arm}}) I_{c0}}{V_d} \right) \int \tilde{i}_c^k) \\ &= \frac{1}{V_d} \left(-R_a \cdot 2V_d \cdot \tilde{i}_d + \frac{N}{C_{\mathrm{sub}}} R_{\mathrm{arm}} I_{c0} \right. \\ &\qquad \left. \times \left(1 + \frac{2(R_a - R_{\mathrm{arm}}) I_{c0}}{V_d} \right) \int \tilde{i}_d \right) \\ &= -2R_a \tilde{i}_d + \left(1 + \frac{2(R_a - R_{\mathrm{arm}}) I_{c0}}{V_d} \right) \frac{N R_{\mathrm{arm}} I_{c0}}{V_d C_{\mathrm{sub}}} \int \tilde{i}_d. \end{aligned} \tag{40}$$

Substituting (26), (36), (39), and (40) into (25) yields

$$\begin{aligned} &2L_{\mathrm{arm}} \frac{d\tilde{i}_d}{dt} + \frac{N}{2C_{\mathrm{sub}}} \left(1 + \frac{2(R_a - R_{\mathrm{arm}}) I_{c0}}{V_d} \right) \int \tilde{i}_d \\ &- \left(-2R_a \tilde{i}_d + \left(1 + \frac{2(R_a - R_{\mathrm{arm}}) I_{c0}}{V_d} \right) \frac{N R_{\mathrm{arm}} I_{c0}}{V_d C_{\mathrm{sub}}} \int \tilde{i}_d \right) \\ &+ 2R_{\mathrm{arm}} \tilde{i}_d = 3\tilde{v}_d \rightarrow \frac{\tilde{v}_d(s)}{\tilde{i}_d(s)} = \frac{2sL_{\mathrm{arm}}}{3} + \frac{2}{3}(R_a + R_{\mathrm{arm}}) \\ &+ \frac{N}{6sC_{\mathrm{sub}}} \left(1 + \frac{2(R_a - R_{\mathrm{arm}}) I_{c0}}{V_d} \right) \left(1 - \frac{2R_{\mathrm{arm}} I_{c0}}{V_d} \right). \end{aligned} \tag{41}$$

Compared to (37), the dc equivalent impedance is still linear at the second-harmonic frequency, and an MMC can also be considered as a series connected *R–L–C* branch, while the equivalent resistance and capacitance vary with the proportional coefficient R_a selected in the circulating current control.

In practice, PR control with resonance frequency of 120 Hz (second order), instead of proportional control, may be used to suppress circulating current under normal and unbalanced conditions. Under such circumstances, the derived equivalent dc impedance in (41) is still applicable. The only modification is that R_a in (41) should be replaced by the gain of the PR controller at the resonant frequency.

Based on (37) and (41), the equivalent circuit of the zero-sequence circulating current i_c^0 in an MMC-HVdc is shown in Fig. 6. The double-line frequency dc current ripple, which equals to 3 i_c^0, is suppressed by both dc cable impedance (Z_{cable}) and dc-side equivalent impedance of MMC inverter (Z_{mmc}). Therefore, in a system with long dc cables and/or high circulating

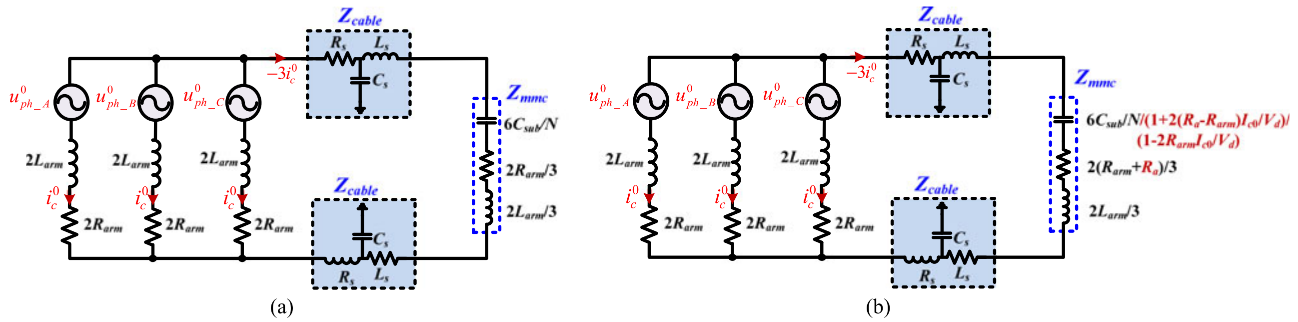

Fig. 6. Equivalent circuit of the second-order dc voltage ripple under SLG fault conditions. (a) Without circulating current control. (b) With circulating current control.

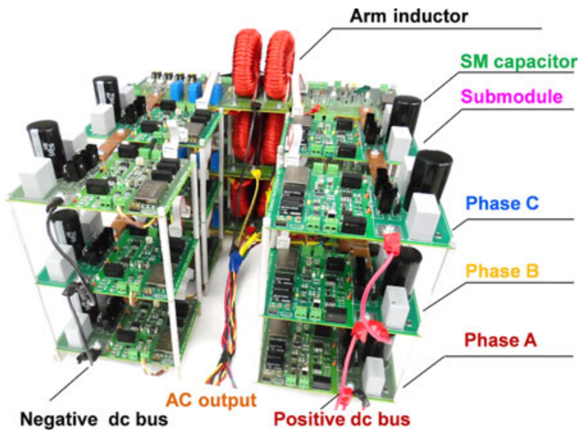

Fig. 7. Prototype of scaled-down three-phase MMC inverter.

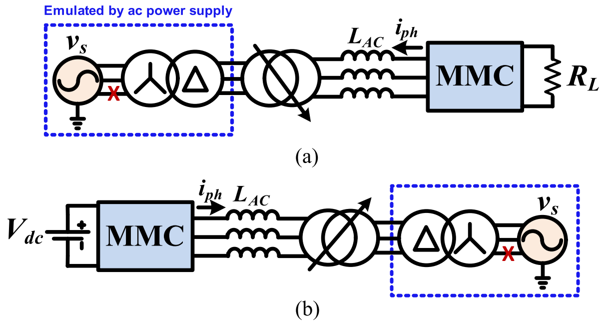

Fig. 8. Configuration of the experimental system with phase C open.

TABLE I
Main Circuit Parameters of MMC Prototype

Parameters	Values	Parameters	Values
Max. DC Link voltage $V_{\rm dc}$	150 V	No. of SMs per phase	4
Voltage frequency	60 Hz	SM capacitance $C_{\rm sub}$	2200 μF
Arm inductance $L_{\rm arm}$	0.74 mH	Carrier frequency f_c	1 kHz
Arm inductor ESR $R_{\rm arm}$	0.06 Ω	DC-side inductance $L_{\rm dc}$	0.45 mH
AC-side inductance $L_{\rm AC}$	1.8 mH	ESR of DC inductance $R_{\rm dc}$	0.05 Ω
Equivalent resistance of AC inductors	0.09 Ω	Load resistance R_L	30 Ω

current control coefficient R_a, no obvious second-order current ripple will be found in the dc current under SLG fault conditions.

As shown in (9) and (15), the elimination of i_c^0 will reduce but cannot remove the second-order phase voltage ripple on the dc cables and MMC inverter. This voltage ripple may lead to distorted ac voltage in MMC_2 station through modulation and feedback control loops, which requires additional control schemes to mitigate. If the converter regulating dc voltage suffers unbalanced ac voltages, dc voltage V_d in (23)–(32) cannot be regarded as a constant value, and the corresponding voltage regulators should be considered in the dc impedance derivation.

With the derived steady-state model, the arm inductance and SM capacitance can be designed theoretically to mitigate the circulating current under unbalanced conditions, thus reducing the current stress imposed on power devices and passive components. Moreover, the steady-state model can help the circulating current controller design and maximum modulation index calculation, using the same methodology discussed in [40] and [41] for balanced conditions.

In addition, since the steady-state model is derived based on the generic inner relationships among current and voltage quantities, it is applicable to any unbalanced conditions, including SLG fault. Nevertheless, if the system is not equipped with SPS, or a permanent SLG fault or other asymmetrical (e.g., line-to-line, line-to-lint-to-ground) fault occurs, the protection will be tripped and disconnect the MMC-HVdc system from the ac grid in several cycles, before the steady state is arrived. Therefore, the derived model could be mainly used for unbalanced conditions, where no relay protection is involved and the system can maintain continuous operation.

V. Experimental Verification

To verify the theoretical analysis and developed impedance model, a scaled-down three-phase MMC is built, as shown in Fig. 7. Given that the number of SMs has little impact on the model verification, four cells per phase are used in this paper to achieve low hardware requirement. The control schemes are implemented by dSPACE DS1103 and FPGA (Cyclone IV DE0-Nano). For high equivalent switching frequency and relatively simple implementation, the $N+1$ level phase shift PWM modulation scheme is adopted. Additionally, the widely used capacitor voltage sorting and balancing control is applied to guarantee operation performance of MMC under both normal as well as unbalanced conditions.

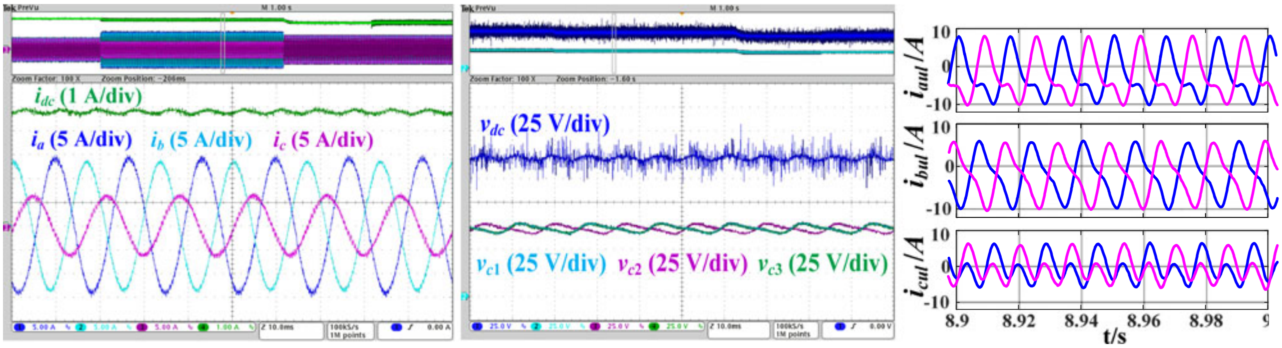

(a) (b) (c)

Fig. 9. Experimental results of an MMC rectifier under SLG fault, with only positive-sequence current control. (a) Converter-side phase current and dc current. (b) Capacitor voltage in phase A and dc voltage. (c) Three-phase arm currents.

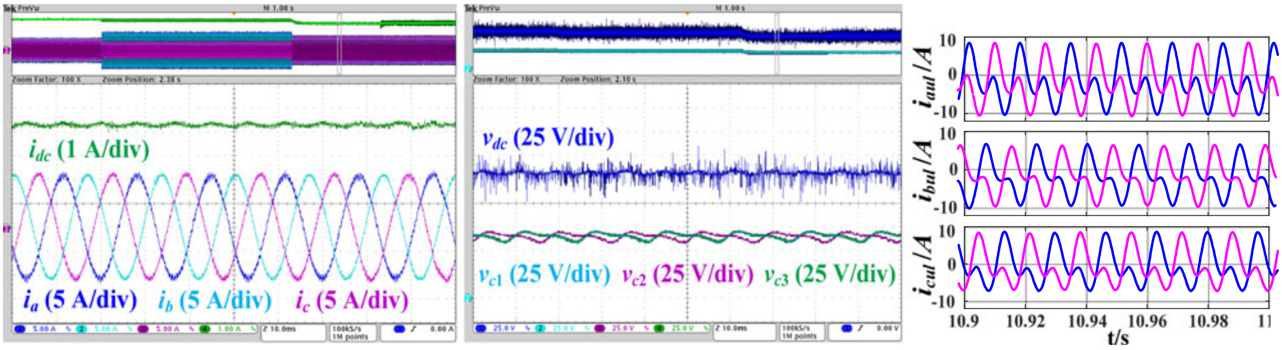

(a) (b) (c)

Fig. 10. Experimental results of an MMC rectifier under SLG fault, with negative-sequence current control. (a) Converter-side phase current and dc current. (b) Capacitor voltage in phase A and dc voltage. (c) Three-phase arm currents.

Three cases, including MMC rectifier with resistive load under SLG fault, MMC inverter with resistive load under SLG fault, and MMC inverter with second-order voltage ripple in dc side (emulate point to point MMC-HVdc), are studied. To create serious unbalanced grid conditions, an SLG fault is emulated by setting phase C voltage to zero by an ac power supply (FCS Series II by California Instruments). The corresponding voltage and current characteristics in the converter side are similar to that of a real system suffering SLG fault and have ungrounded neutral point in the Y side of the transformer. Although this setup has lower unbalanced voltage and current if compared to the system with grounded neutral point in the Y side, it still could provide a verification of the proposed steady-state model, while not triggering any overcurrent and grounding current protection. For convenience, the "SLG fault" mentioned in the following analysis refers to this emulation.

A. MMC Rectifier With Resistive Load Under SLG Fault

The configuration of the MMC rectifier is illustrated in Fig. 8(a), and its main circuit parameters are given in Table I. To prevent the potential damage or degradation of power semiconductor devices under fault conditions, the current reference is limited to 1.2 times of the rated phase current.

Fig. 9 shows the selected experimental results with only positive-sequence current control. When the SLG fault occurs, converter-side phase current becomes unbalanced because of the negative-sequence component. Meanwhile, the zero-sequence circulating current flows into the dc side, forming a second-order dc current ripple. Its magnitude, however, is only 0.09 A (2.05%) due to the large dc load resistance. The percentage values here and in the following description refer to comparison of current and voltage components to rated dc voltage of 150 V and dc current of 4.98 A. The dc components in the three phase arm currents change from 1.66 A under normal condition to 2.33 A (140.4%), 2.05 A (123.5%), and 0.4 A (24.1%) under SLG fault, which represents uneven active power contributions. Moreover, the three phase arm currents present different shapes and RMS values due to unbalanced phase and circulating current, resulting in unequal power losses across semiconductor devices. The second-order ripple can also be observed in the dc voltage, which has a magnitude of 2.58 V (1.72%). Additionally, due to the lack of dc central capacitors, the switching ripple cannot be filtered as in two level VSCs, which appears in dc voltage and current [see Fig. 9(a) and (b)].

After the negative-sequence current control is activated, converter-side phase current becomes balanced, as shown in Fig. 10(a). This balanced phase current, however, results in a further drop of dc voltage, which reduces from 144.43 V (96.3%) in Fig. 9(b) to 129.81 V (86.54%) in Fig. 10(b). Compared to Fig. 9, the second-order ripple in both dc current and dc voltage are reduced, which are 0.06 A (1.4%) and 1.69 V (1.13%) in

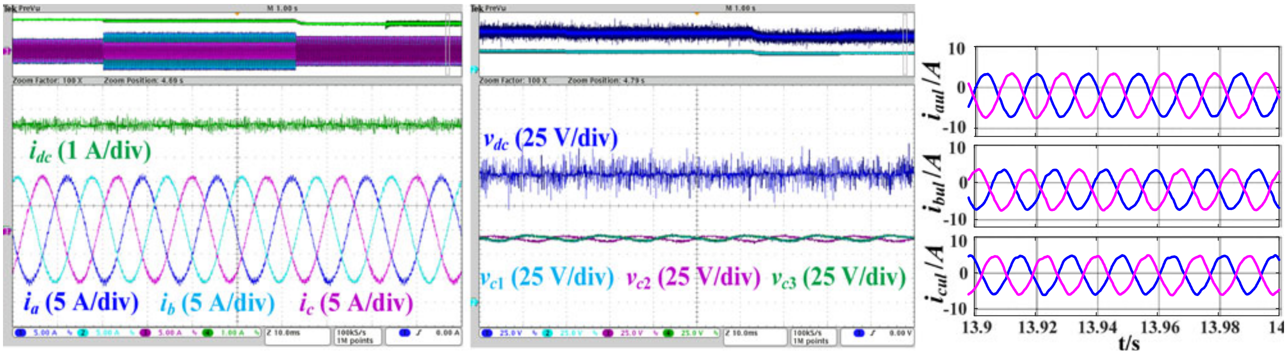

(a) (b) (c)

Fig. 11. Experimental results of an MMC rectifier under SLG fault, with negative-sequence current and circulating current control. (a) Converter-side phase current and dc current. (b) Capacitor voltage in phase A and dc voltage. (c) Three-phase arm currents.

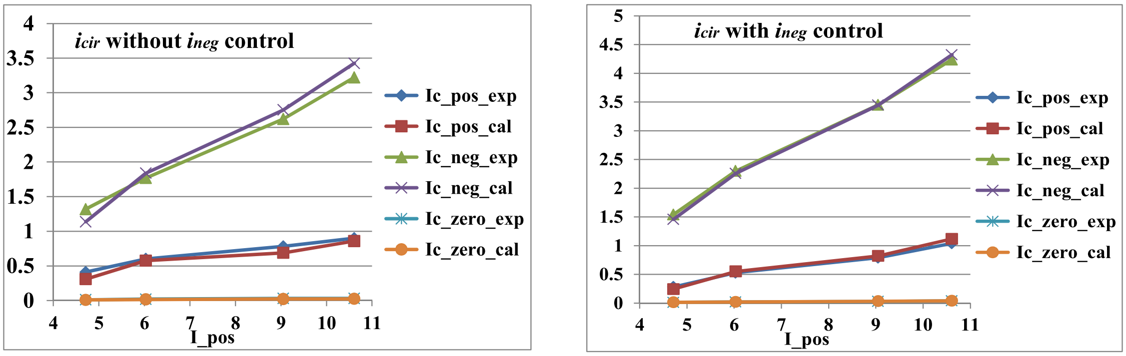

Fig. 12. Comparison between experimental and calculation results of circulating current under SLG fault. (a) Without negative-sequence current control. (b) With negative-sequence current control.

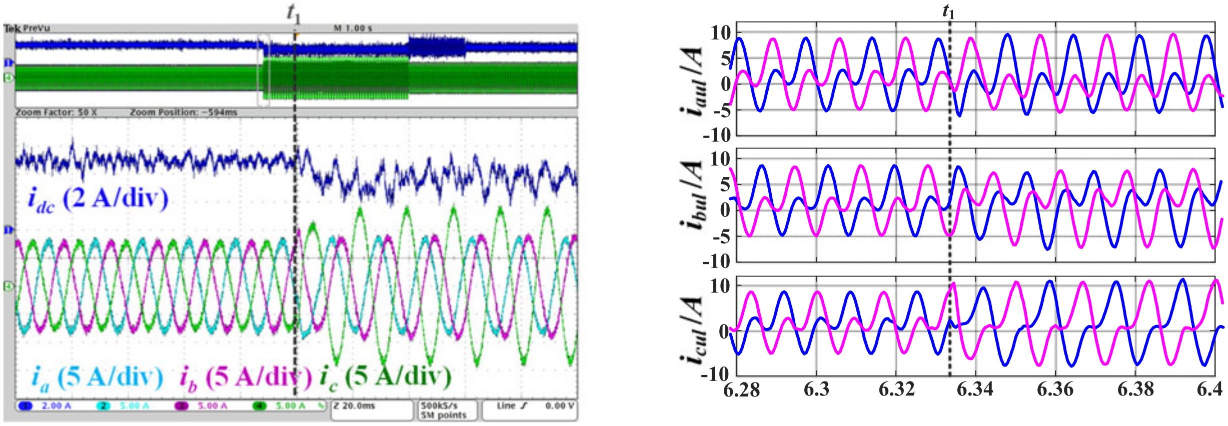

(a) (b)

Fig. 13. Transient performance of an MMC inverter when SLG fault occurs. (a) Converter-side phase current and dc current. (b) Three-phase arm currents.

this case. The dc components in three phase arm current drop to 1.89 A (113.9%), 1.91 A (115.1%), and 0.5 A (30.1%).

Fig. 11 illustrates the experimental results when circulating current control is also activated in *abc* coordinates. The double-line frequency positive-, negative-, and zero-sequence circulating current are greatly suppressed, enabling sinusoidal arm currents and a second-order dc current ripple of 0.01 A (0.2%). In spite of the elimination of circulating current, a second-order dc voltage ripple with magnitude of 0.49 V (0.33%) [see Fig. 11(b)] still exists because of the first four items in the zero-sequence components in (15), which may demand for special designed dc voltage ripple control. The additional switching actions induced by circulating current control add more switching ripple in the dc voltage and current [42].

Fig. 12 shows the comparison between experimental and calculation results of circulating current under SLG fault. When the negative-sequence current control is not activated, a deviation appears between the calculated and tested magnitudes of

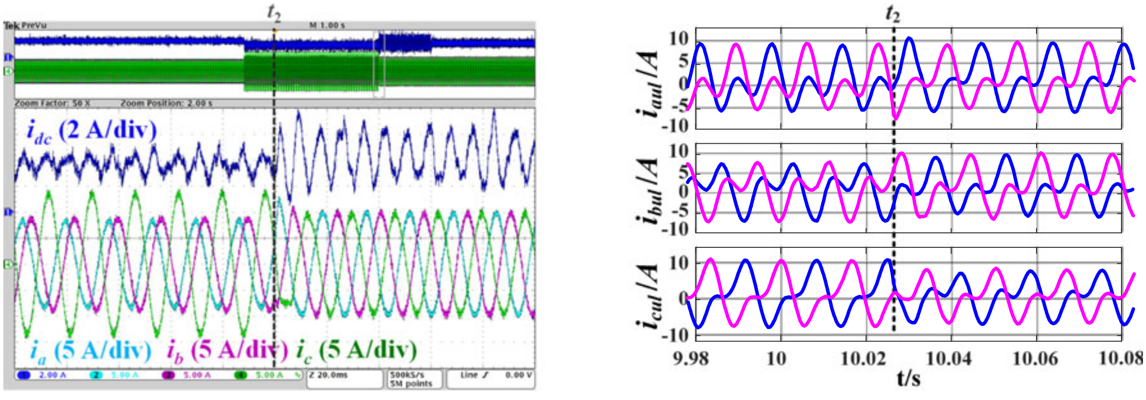

(a) (b)

Fig. 14. Transient performance of an MMC inverter when negative-sequence current control starts. (a) Converter-side phase current and dc current. (b) Three-phase arm currents.

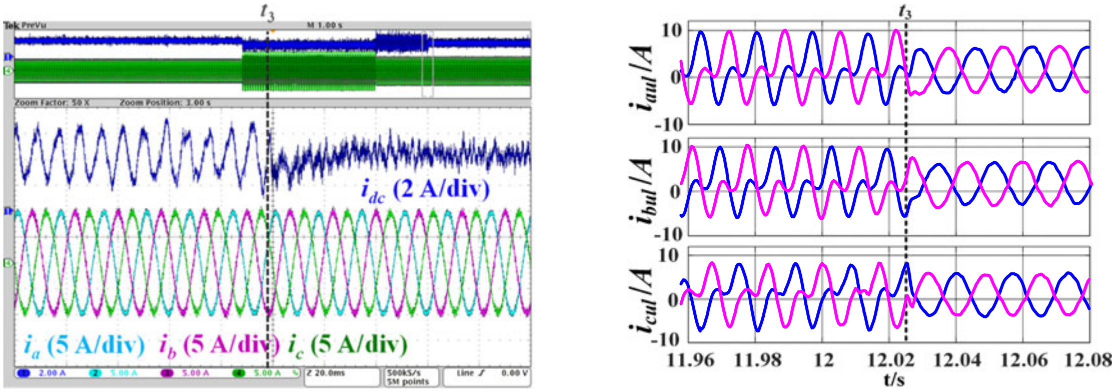

(a) (b)

Fig. 15. Transient performance of an MMC inverter when circulating current control is activated. (a) Converter-side phase current and dc current. (b) Three-phase arm currents.

circulating current. During the derivation of second-order voltage ripple in (9), the negative-sequence modulation index M^- is assumed to be zero. In experiments, nevertheless, a small M^- is introduced by the dc voltage feedback control, which mainly induces the mismatch in Fig. 12(a).

With negative-sequence current control, since the assumption $I^- = 0$ in (13) always holds when dual-current control operates, the mismatch between calculation and experimental results of positive- and negative-sequence circulating current in Fig. 12(b) is greatly reduced within the tested range. The magnitude of zero-sequence circulating current is below 0.04 A in both cases with a dc resistance of 30 Ω. The negative-sequence current control also leads to an apparent magnitude increase of negative- and positive-sequence circulating currents, as shown in Fig. 12(b).

B. MMC Inverter Under SLG Fault

To further verify the derived model, an MMC inverter under SLG fault is also investigated with the same main circuit parameters in Table I, as shown in Fig. 8(b). Since the ac power supply v_s used in the experiment cannot absorb active power, three 5 Ω resistors are connected at the output of the inverter.

Fig. 13 gives the transient performance of an MMC inverter when an SLG fault occurs at t_1. Similar to Fig. 9, the SLG fault leads to unbalanced phase currents and lower active power generation. Consequently, the dc components in three-phase arm current reduce to 1.19 A (71.7%), 1.21 A (72.9%), and 1.33 A (80.1%), respectively. When the negative-sequence current control starts at t_2, the converter-side phase current becomes balanced within a fundamental cycle [see Fig. 14(a)]. However, the magnitude of second-order dc current ripple increases to 4.37 A (87.8%), and active power is more unevenly distributed among three phases, leading to dc arm currents of 1.75(105.4%), 1.73(104.2%), and 0.9 A (54.2%) [see Fig. 14(b)]. When circulating current control is enabled at t_3, the second-order dc current drops to 0.01 A and arm currents become sinusoidal with dc components slightly affected in three phases (see Fig. 15).

Fig. 16 illustrates the comparison between calculation and experimental results of circulating current in an MMC inverter under SLG fault. The mismatch reduces from 0.4 A [see Fig. 16(a)] to less than 0.1 A [see Fig. 16(b)] when the negative-sequence current control is activated. However, due to lower dc impedance $Z_{\mathrm{dc\_eq}}$, variation of phase current and modulation index, the magnitude of negative-sequence component drops a

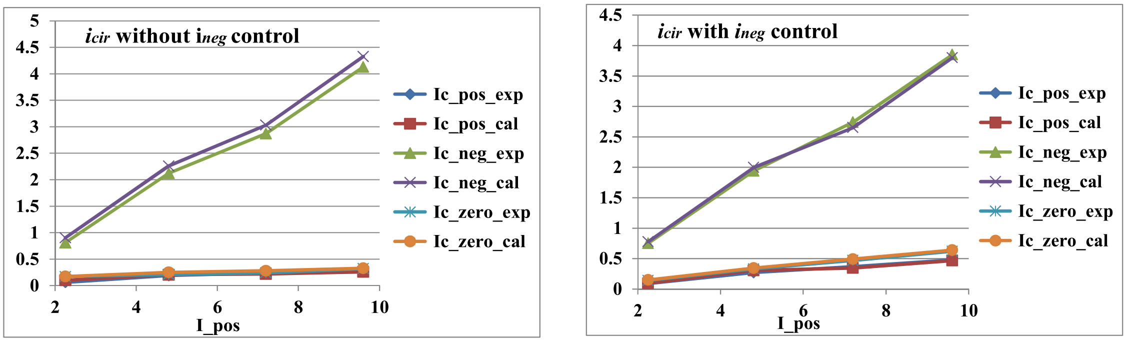

(a) (b)

Fig. 16. Comparison between experimental and calculation results of circulating current under SLG fault. (a) Without negative-sequence current control. (b) With negative-sequence current control.

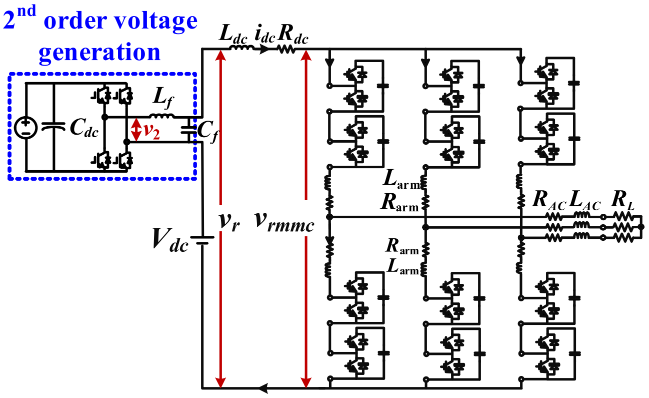

Fig. 17. Configuration of the experimental system.

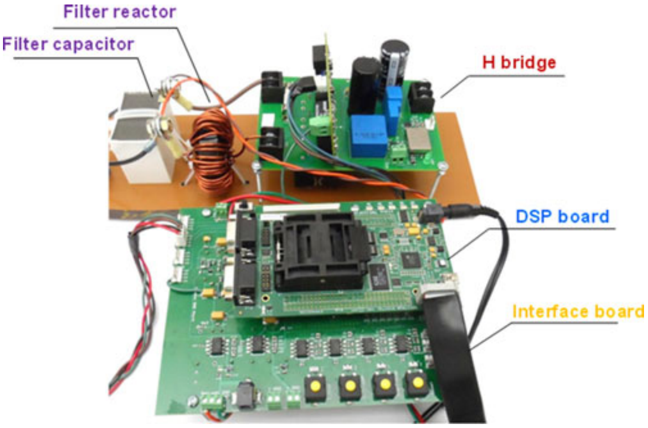

Fig. 18. Second-order voltage source using an H-bridge.

little in this case, while positive- and zero-sequence circulating current has a slight increase.

C. MMC Inverter With Second-Order Voltage Input in DC Side

For simplicity, the point-to-point HVdc in Fig. 1 is separated into a second-order voltage source and an MMC load, as illustrated in Fig. 17. An H-bridge converter controlled by DSP (TMS320F28335) in Fig. 18 is used as the second-order voltage source to emulate the dc voltage ripple under SLG fault condition in the rectifier station. The MMC inverter in Fig. 7 is employed to verify the derived dc equivalent impedance, and its main parameters are the same as Table I except the dc-link voltage $V_{\rm dc} = 100$ V. A dc reactor of 0.45 mH is used for cable impedance emulation.

Figs. 19 and 20 show the selected open-loop experimental results when the proportional coefficient $R_a = 0$, and the second-order dc voltage ripple v_2 has magnitudes of 6 and 12 V, respectively. Compared to Fig. 19, the second-order harmonic in the ac component of $v_{\rm rmmc}$ $(v_{\rm rmmc\_ac})$ has an evident increase with higher v_2 (v_{r_ac}) (Fig. 20(a)), and the second-order dc-side current $i_{\rm dc}$ also becomes much larger [see Fig. 20(a)]. Fig. 21 illustrates the open-loop experimental results with proportional coefficient $R_a = 3$ when the magnitude of v_2 is set to 12 V. As can be observed, although larger R_a induces higher $v_{\rm rmmc\_ac}$, it helps to achieve smaller second-order dc-side current and more sinusoidal arm currents. Additionally, the unbalanced phase current in Fig. 20(b) is also suppressed.

Fig. 22 shows the phase and dc-side current with current loop control when $v_2 = 12$ V. The dominant third-order harmonics in the phase current generated by the second-order dc voltage ripple decreases from 1.43% to 1.09%, and it can be further reduced by increasing the bandwidth and low frequency gain of the current control loop. Comparing Fig. 21(b) with Fig. 22(b), the double-line frequency dc current ripple has almost the same magnitude, which verifies that the control schemes impact only slightly the derived dc equivalent impedance.

Fig. 23 shows the comparison between experimental and calculated results with and without circulating current control. In both cases, the errors of 2nd order MMC dc terminal voltage $(v_{\rm rmmc\_2nd})$ and dc-side current $(i_{\rm dc\_2nd})$ are less than 1% within the plotted range, no matter what control method (open-loop or current loop control) is applied.

Compared to Fig. 23(a), the large impedance brought by the circulating current control in Fig. 23(b) helps to reduce the mismatch caused by dead time, harmonics extraction, cable impedance, parameters tolerance of passive components, etc. Furthermore, high R_a also effectively mitigates $i_{\rm dc\_2nd}$ and reduces the impact of SLG fault on arm currents and capacitor voltage ripples.

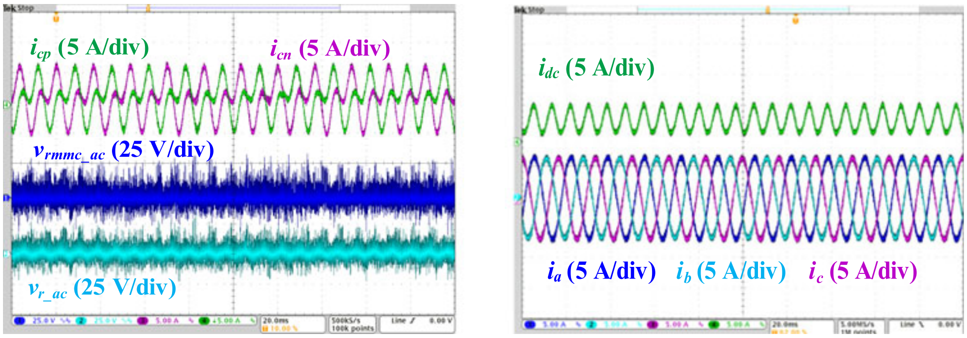

(a) (b)

Fig. 19. Open-loop experimental waveforms with $v_2 = 6$, $R_a = 0$. (a) Arm currents, ac components of $v_{\rm rmmc}$ and v_r. (b) DC-side current and output phase current.

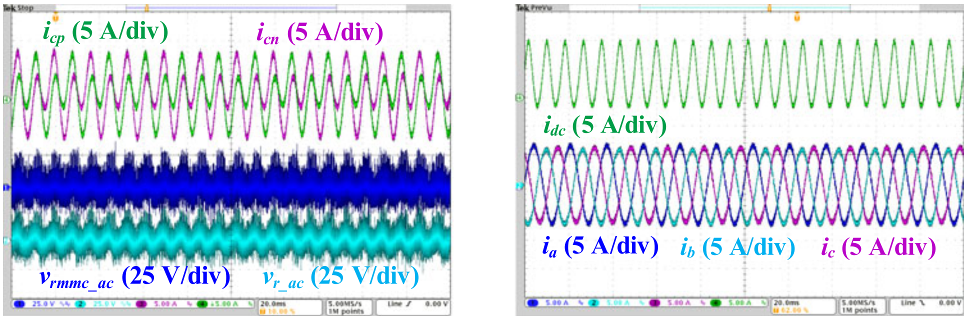

(a) (b)

Fig. 20. Open-loop experimental waveforms with $v_2 = 12$, $R_a = 0$. (a) Arm currents, ac components of $v_{\rm rmmc}$ and v_r. (b) DC-side current and output phase current.

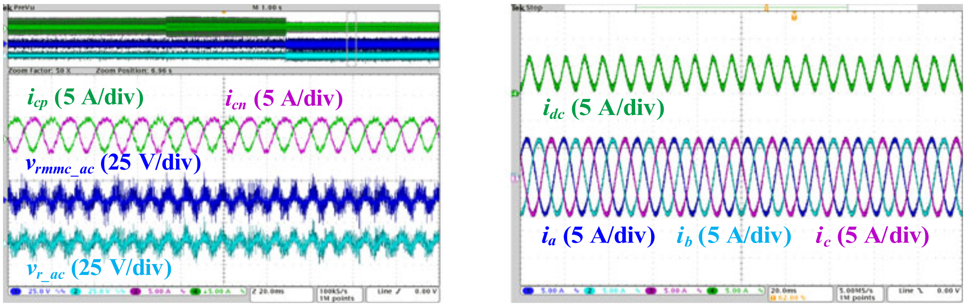

(a) (b)

Fig. 21. Open-loop experimental waveforms with $v_2 = 12$, $R_a = 3$. (a) Arm currents, ac components of $v_{\rm rmmc}$ and v_r. (b) DC-side current and output phase current.

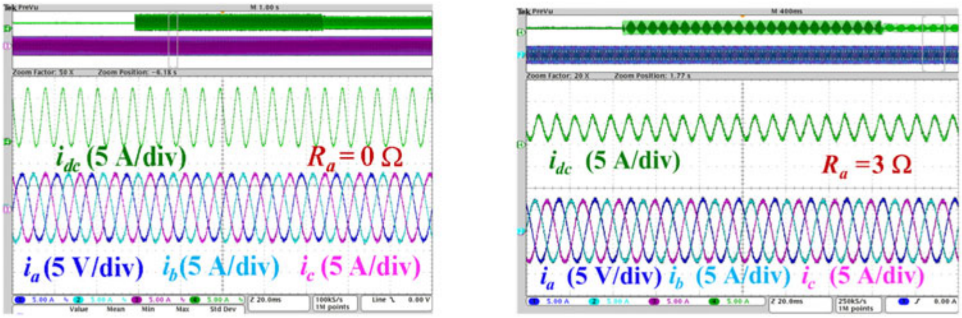

(a) (b)

Fig. 22. Current loop control experimental waveforms with $v_2 = 12$. (a) $R_a = 0$. (b) $R_a = 3$.

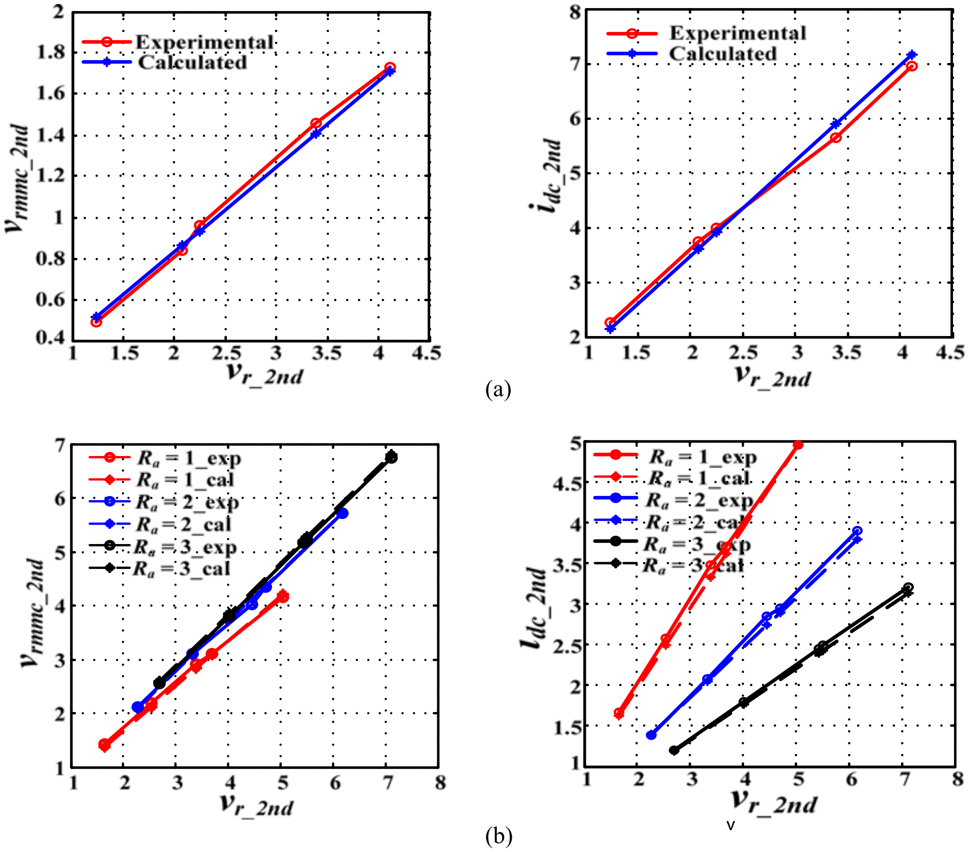

(a)

(b)

Fig. 23. Comparison between experimental and calculated results. (a) Without circulating current control. (b) With circulating current control.

VI. CONCLUSION

This paper presents a steady-state model of the MMC to predict the system performance under unbalanced conditions. The model is derived and experimentally verified, considering the impact of negative-sequence current control, circulating current control, and different load conditions. The key points in this paper can be summarized as follows:

1) A steady-state model that describes the relationship between current and voltage quantities of MMC under unbalanced conditions is proposed. The sources of negative-, positive-, and zero-sequence circulating current are provided, and dc components in three-phase circulating current, which deviate from each other due to the existence of negative-sequence current or modulation index, can be calculated theoretically.
2) A detailed comparison of the proposed model with/without negative-sequence current control reveals that when the widely used dual-current control is applied, the positive-, negative-, and zero-sequence circulating current are generated by more voltage sources and are no longer decoupled.
3) According to the circular relationship found from the steady-state model, the magnitudes and initial phase angles of different circulating current components can be easily predicted. Moreover, the fundamental and low-frequency harmonic components of the capacitor charging currents, capacitor voltages, arm currents, and output phase voltages can be analytically expressed.
4) The equivalent dc impedance of the MMC is first derived for circulating current calculation in a point to point MMC-HVdc system. Based on the derivation, an MMC inverter can be represented as a series-connected *R*–*L*–*C* branch, and the equivalent resistance and capacitance depend on circulating current control parameters.
5) The derived steady-state models are verified in a three-phase scaled-down MMC rectifier and inverter prototype under an emulated SLG fault. Moreover, verification of the equivalent dc impedance is achieved by injecting a second-order ripple into the dc link of an MMC inverter. The comparison between experimental and calculation results under three kinds of test conditions demonstrate the validity of the analysis and derivation.

In order to further verify the aforementioned contributions, several more scenarios could be tested in the future:

1) Determine a practical way to completely decouple the positive- and negative-sequence current in order to mitigate the mismatch between calculated and experimental results.
2) Vary the voltage unbalance ratio by adjusting the three-phase output voltage, measure the corresponding circulating current, and compare it with the calculated values.

3) Measure circulating currents with different arm inductances as well as SM capacitances, and compare them with the calculated values.

REFERENCES

[1] K. Friderich, "Modern HVDC PLUS application of VSC in modular multilevel converter topology," in *Proc. Int. Symp. Ind. Electron.*, Jul. 2010, pp. 3807–3810.

[2] S. Allebrod, R. Hamerski, and R. Marquardt, "New transformerless, scalable modular multilevel converters for HVDC-transmission," in *Proc. IEEE Power Electron. Spec. Conf.*, 2008, pp. 174–179.

[3] H. Akagi, "Classification, terminology, and application of the modular multilevel cascade converter (MMCC)," *IEEE Trans. Power Electron.*, vol. 26, no. 11, pp. 3119–3130, Nov. 2011.

[4] S. Teeuwsen, "Modeling the Trans Bay cable project as voltage-sourced converter with modular multilevel converter design," in *Proc. IEEE Power Energy Soc. Annu. Meeting*, Jul. 2011, pp. 1–8.

[5] M. Saeedifard and R. Iravani, "Dynamic performance of a modular multilevel back-to-back HVDC system," *IEEE Trans. Power Del.*, vol. 25, no. 4, pp. 2903–2912, Oct. 2010.

[6] A. Antonopoulos, L. Angquist, and H.-P. Nee, "On dynamics and voltage control of the modular multilevel converter," in *Proc. Eur. Conf. Power Electron. Appl.*, 2009, pp. 1–10.

[7] K. Ilves, S. Norrga, L. Harnefors, and H.-P. Nee, "On energy storage requirements in modular multilevel converters," *IEEE Trans. Power Electron.*, vol. 29, no. 1, pp. 77–88, Jan. 2014.

[8] E. Solas, G. Abad, J. Barrena, S. Aurtenechea, A. Carcar, and L. Zajac, "Modular multilevel converter with different subomodule concepts-Part II: Experimental validation and comparison for HVDC application," *IEEE Trans. Ind. Electron.*, vol. 60, no. 10, pp. 4536–4545, Oct. 2013.

[9] Q. Tu, Z. Xu, and L. Xu, "Reduced switching-frequency modulation and circulating current suppression for modular multilevel converter," *IEEE Trans. Power Del.*, vol. 26, no. 3, pp. 2009–2017, Jul. 2012.

[10] K. Ilves, L. Harnefors, S. Norrga, and H.-P. Nee, "Predictive sorting algorithm for modular multilevel converters minimizing the spread in the submodule capacitor voltages," *IEEE Trans. Power Electron.*, vol. 30, no. 1, pp. 440–449, Jan. 2015.

[11] F. Deng and Z. Chen, "A control method for voltage balancing in modular multilevel converters," *IEEE Trans. Power Electron.*, vol. 29, no. 1, pp. 66–76, Jan. 2014.

[12] M. Guan and Z. Xu, "Modeling and control of a modular multilevel converter-based HVDC system under unbalanced grid conditions," *IEEE Trans. Power Electron.*, vol. 27, no. 12, pp. 4858–4867, Dec. 2012.

[13] Q. Tu, Z. Xu, Y. Chang, and L. Guan, "Suppressing DC voltage ripples of MMC-HVDC under unbalanced grid conditions," *IEEE Trans. Power Del.*, vol. 27, no. 3, pp. 1332–1338, Jul. 2012.

[14] J. Moon, C. Kim, J. Park, D. Kang, and J. Kim, "Circulating current control in MMC under the unbalanced voltage," *IEEE Trans. Power Del.*, vol. 28, no. 3, pp. 1952–1959, Jul. 2013.

[15] Y. Zhou, D. Jiang, J. Guo, P. Hu, and Y. Liang, "Analysis and control of modular multilevel converters under unbalanced conditions," *IEEE Trans. Power Electron.*, vol. 28, no. 4, pp. 1986–1995, Oct. 2013.

[16] ABB, "It's time to connect," (2012). [Online]. Available: http://new.abb.com/docs/default-source/ewea-doc/hvdc-light.pdf?sfvrsn=2

[17] Y. Ma *et al.*, "System scheme of Zhoushan multi-terminal VSC-HVDC project," *Elect. Power Construction*, vol. 35, no. 3, pp. 1–6, Mar. 2014.

[18] H. Saad, S. Dennetiere, C. Lallemand, B. Clerc, and Y. Vernay, "Commissioning of the France Spain HVDC VSC control system replicas," in *Proc. CIGRE-IEC Colloquium*, 2016, pp. 1–8.

[19] P. Damgaard, "HVDC schemes under construction or planned," Cigre, B4.

[20] Cigre, B4, "BorWin2 HVDC system," (2015). [Online]. Available: http://b4.cigre.org/Publications/Other-Documents/Compendium-of-all-HVDC-projects/BorWin2-HVDC-System

[21] L. Ängquist, A. Antonopoulos, and H.-P. Nee, "On dynamics and voltage control of the modular multilevel converter," in *Proc. Eur. Conf. Power Electron. Appl.*, Barcelona, Spain, 2009, pp. 1–10.

[22] H. Song and K. Nam, "Dual current control scheme for PWM converter under unbalanced input voltage conditions," *IEEE Trans. Ind. Electron.*, vol. 46, no. 5, pp. 953–959, Oct. 1999.

[23] B. Parkhideh and S. Bhattacharya, "Vector-controlled voltage-source-converter-based transmission under grid disturbances," *IEEE Trans. Power Electron.*, vol. 28, no. 2, pp. 661–672, Feb. 2013.

[24] P. Rodríguez, A. Luna, I. Candela, R. Mujal, R. Teodorescu, and F. Blaabjerg, "Multiresonant frequency-locked loop for grid synchronization of power converters under distorted grid conditions," *IEEE Trans. Ind. Electron.*, vol. 58, no. 1, pp. 127–138, Jan. 2011.

[25] X. Shi, Z. Wang, B. Liu, Y. Liu, L. M. Tolbert, and F. Wang, "Characteristic investigation and control of modular multilevel converter based HVDC system under single-line-to-ground fault conditions," *IEEE Trans. Power Electron.*, vol. 30, no. 1, pp. 408–421, Jan. 2015.

[26] L. Xiao, S. Huang, and K. Lu, "DC-bus voltage control of grid-connected voltage source converter by using space vector modulated direct power control under unbalanced network conditions," *IET Power Electron.*, vol. 6, no. 5, pp. 925–934, 2013.

[27] Y. Suh and T. A. Lipo, "Control scheme in hybrid synchronous stationary frame for PWM AC/DC converter under generalized unbalanced operating conditions," *IEEE Trans. Ind. Appl.*, vol. 42, no. 3, pp. 825–835, May/Jun. 2006.

[28] J. Hu and Y. He, "Modeling and control of grid-connected voltage-sourced converters under generalized unbalanced operation conditions," *IEEE Trans. Energy Convers.*, vol. 23, no. 3, pp. 903–913, Sep. 2008.

[29] A. Yazdani and R. Iravani, "A unified dynamic model and control for the voltage-sourced converter under unbalanced grid conditions," *IEEE Trans. Power Del.*, vol. 21, no. 3, pp. 1620–1629, Jul. 2006.

[30] V. H. Serna Reyna, J. C. Rivera Velázquez, H. E. Prado Félix, H. J. Altuve Ferrer, D. Sánchez scobedo, and J. Gallegos Guerrero, "Transmission line single-pole tripping: field experience of the western transmission area of Mexico," in *Proc. of the 37th Annu. Western Protective Relay Conf.*, Spokane, WA, USA, Oct. 2010, pp. 1–12.

[31] Z. M. Radojeviç and J. R. Shin, "New digital algorithm for adaptative reclosing based on the calculation of the faulted phase voltage total harmonic distortion factor," *IEEE Trans. Power Del.*, vol. 22, no. 1, pp. 37–41, Jan. 2007.

[32] E. Godoy, A. Celaya, H. J. Altuve, N. Fischer, and A. Guzmán, "Tutorial on single-pole tripping and reclosing," in *Proc. of the 39th Annu. Western Protective Relay Conf.*, Spokane, WA, USA, Oct. 2012, pp. 1–21.

[33] A. G´omez-Exp´osito, A. J. Conejo, and C. Ca˜nizares, *Electric Energy Systems - Analysis and Operation*. Boca Raton, FL, USA: CRC Press, 2009, ISBN 978-0-8493-7365-7.

[34] A. R. Bergen and V. Vittal, *Power Systems Analysis*, 2nd ed. Englewood Cliffs, NJ, USA: Prentice-Hallc., 2000, p. 619, ISBN 0-13-691990-1.

[35] P. M. Anderson, *Analysis of Faulted Power Systems*. New York, NY, USA: Wiley-IEEE Press, 1995.

[36] H. Saadat, *Power System Analysis*, 3rd ed. London, U.K.: PSA Publishing LLC, 2011.

[37] Q. Song, W. Liu, X. Li, H. Rao, S. Xu, and L. Li, "A steady-state analysis method for a modular multilevel converter," *IEEE Trans. Power Electron.*, vol. 28, no. 8, pp. 3702–3713, Aug. 2013.

[38] L. Harnefors, A. Antonopoulos, S. Norrga, L. Ängquist, and H.-P. Nee, "Dynamic analysis of modular multilevel converters," *IEEE Trans. Ind. Electron.*, vol. 60, no. 7, pp. 2526–2537, Jul. 2013.

[39] A. Antonopoulos, L. Ängquist, L. Harnefors, K. Ilves, and H.-P.Nee, "Global asymptotic stability of modular multilevel converters," *IEEE Trans. Ind. Electron.*, vol. 61, no. 2, pp. 603–612, Feb. 2014.

[40] Q. Tu, Z. Xu, and X. Lie, "Reduced switching-frequency modulation and circulating current suppression for modular multilevel converter," *IEEE Trans. Power Del.*, vol. 26, no. 3, pp. 2009–2017, Jul. 2012.

[41] Y. Li, X. Shi, B. Liu, F. Wang, and W. Lei, "Maximum modulation index for modular multilevel converter with circulating current control," in *Proc. IEEE Energy Convers. Congr. Expo.*, 2014, pp. 491–498.

[42] Y. Li, E. A. Jones, and F. Wang, "Switching-frequency ripple on DC link voltage in a modular multilevel converter with circulating current suppressing control," in *Proc. IEEE Appl. Power Electron. Conf. Expo.*, 2014, pp. 191–195.

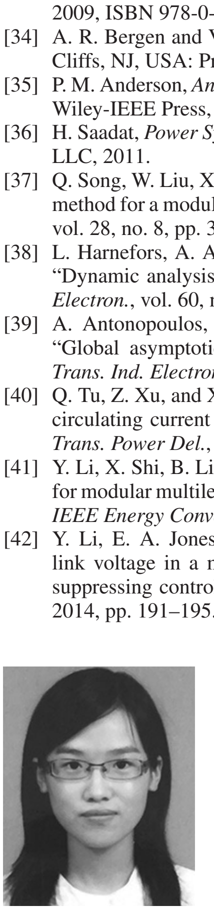

Xiaojie Shi (S'11) received the M.S. degree from Zhejiang University, Hangzhou, China, in 2011, and the Ph.D. degree from the University of Tennessee, Knoxville, TN, USA, in 2015, both in electrical engineering.

She is currently a Research Assistant Professor in the Center for Ultra-Wide-Area Resilient Electric Energy Transmission Networks, University of Tennessee. Her research interests include microgrid, high-power grid-connected converters, HVdc transmission systems, and integration of distributed energy resources.

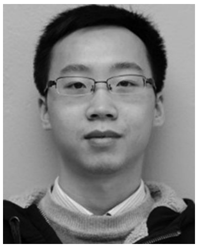

Zhiqiang (Jack) Wang (S'11–M'15) received the B.S. degree from Hunan University, Changsha, China, in 2007 and the M.S. degree from Zhejiang University, Hangzhou, China, in 2010, both in electrical engineering. He started working toward the Ph.D. degree in electrical engineering from the Center for Power Electronics Systems, Virginia Tech, Blacksburg, VA, USA, in 2010, and in 2011, he transferred to the Center for Ultra-Wide-Area Resilient Electric Energy Transmission Networks, University of Tennessee, Knoxville, TN, USA, where he received the Ph.D. degree in 2015.

He is an R&D staff member in the Power Electronics and Electric Machinery Group, Oak Ridge National Laboratory, Oak Ridge, TN, USA. He joined the Post-Master's Program with the Power Electronics and Electric Machinery Research Center, Oak Ridge National Laboratory in 2014 and became a staff member in 2015. His research interests include high-power grid-connected converters, high-temperature high-density power conversion, driving/protection/packaging/integration of wide bandgap devices, and wireless power transfer.

Dr. Wang currently serves as an Associate Editor for the IEEE TRANSACTIONS ON INDUSTRY APPLICATIONS.

Bo Liu (S'11) received the B.S. and M.S. degrees in electrical engineering from Xi'an Jiaotong University, Xi'an, China, respectively, in 2009 and 2012. He is currently working toward the Ph.D. degree in electrical engineering in the Center for Ultra-Wide-Area Resilient Electric Energy Transmission Networks, University of Tennessee, Knoxville, TN, USA.

His current research interests include hybrid ac/dc transmission system, grid emulation, GaN-based high-frequency high-density three-phase rectifier, and conducted EMI.

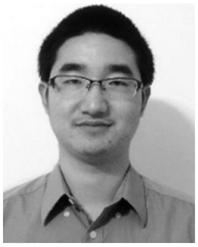

Yalong Li (S'12) received the B.S. degree in electrical engineering from Huazhong University of Science and Technology, Wuhan, China, in 2011. He received the M.S. degree in electrical engineering from The University of Tennessee, Knoxville, TN, USA, in 2013, and is currently working toward the Ph.D. degree in electrical engineering from The University of Tennessee, Knoxville, TN.

He has been with the Center for Ultra-Wide-Area Resilient Electric Energy Transmission Networks, University of Tennessee, Knoxville, TN, USA, since then. His research interests include modular multilevel converters and high voltage dc transmission.

Leon M. Tolbert (S'87–M'91–SM'97–F'13) received the bachelor's, M.S., and Ph.D. degrees in electrical engineering from Georgia Tech, Atlanta, GA, USA, in 1989, 1991, and 1999, respectively.

He joined Oak Ridge National Laboratory in 1991 and worked on several electrical distribution projects at three U.S. Department of Energy Plants, Oak Ridge, TN, USA, from 1991 to 1999. He joined the University of Tennessee in 1999 and is currently the Min H. Kao Professor and the Department Head in electrical engineering and computer science. He is a founding member and thrust leader of CURENT, the NSF/DOE Engineering Research Center established at UT in 2011 to examine the structure and control of future electric grids. He is also a part time Senior Research Engineer at ORNL and conducts joint research in the Power Electronics and Electric Machinery Research Center. He does research in the areas of electric power conversion for renewable energy sources, multilevel converters, utility application of power electronics, microgrids, electric vehicles, and application of wide bandgap (SiC and GaN) power electronics.

Dr. Tolbert is a registered Professional Engineer in the State of Tennessee. He was elected as a member-at-large to the IEEE Power Electronics Society Advisory Committee for 2010–2012, and has served as the Chair of the PELS Membership Committee and Education Committee. He was an Associate Editor of the IEEE TRANSACTIONS ON POWER ELECTRONICS from 2007 to 2012. He has been the Transactions Review Chair for the IEEE TRANSACTIONS ON INDUSTRY APPLICATIONS for the Industrial Power Converter Committee since 2014. He is the coauthor of six IEEE papers that have won prize paper awards.

Fred Wang (S'85–M'91–SM'99–F'10) received the B.S. degree from Xi'an Jiaotong University, Xi'an, China, and the M.S. and Ph.D. degrees from the University of Southern California, Los Angeles, CA, USA, in 1982, 1985, and 1990, respectively, all in electrical engineering.

He was a Research Scientist in the Electric Power Lab, University of Southern California, from 1990 to 1992. He joined the GE Power Systems Engineering Department, Schenectady, NY, USA, as an Application Engineer in 1992. From 1994 to 2000, he was a Senior Product Development Engineer with GE Industrial Systems, Salem, VA, USA. During 2000 to 2001, he was the Manager of Electronic & Photonic Systems Technology Lab, GE Global Research Center, Schenectady and Shanghai, China. In 2001, he joined the Center for Power Electronics Systems, Virginia Tech, Blacksburg, VA, USA, as a Research Associate Professor and became an Associate Professor in 2004. From 2003 to 2009, he also served as the CPES Technical Director. Since 2009, he has been with the University of Tennessee and Oak Ridge National Lab, Knoxville, TN, USA, as a Professor and the Condra Chair of Excellence in power electronics. He is a founding member and the Technical Director of the multiuniversity NSF/DOE Engineering Research Center for Ultra-Wide-Area Resilient Electric Energy Transmission Networks led by the University of Tennessee. His research interests include power electronics, power systems, controls, electric machines, and motor drives.